nature research

https://doi.org/10.1038/s41586-020-3028-8

Supplementary information

Strongly correlated Chern insulators in magic-angle twisted bilayer graphene

In the format provided by the authors and unedited

Supplementary Information: Strongly Correlated Chern Insulators in MATBG

Table of Contents:

A. Topographic identification of the hBN-graphene lattice misalignment
B. High-resolution DT-STS at 200 mK and low magnetic fields
C. Higher-index Landau levels near charge neutrality
D. Magnetic-field dependence of zeroth Landau level quartet splitting
E. Effects of local STM tip potential on spectroscopic gap measurements: charging energy and Coulomb diamonds
F. Raw d*I*/d*V*(V_s,V_g) as a function of magnetic field for Devices B and C
G. Quantized field response of strongly correlated Chern gaps in Devices B and C
H. Method used to reparametrize spectroscopic gap information as a function of filling and fluxes per unit cell
I. Least squares analysis for the Diophantine equation
J. Spectroscopic gap location and error extraction
K. Chern insulating states: Staggered potential mass vs. Haldane mass
L. Free energy argument for the extremal Chern number phases
M. Phenomenological model of DT-STS data at high magnetic fields
N. Quantum Hall ferromagnetism in the zeroth Landau level

A. Topographic identification of the hBN-graphene lattice misalignment

Fig. S1 shows STM topographic images of Device A (Fig. S1a; same as main text Fig. 1a) and Device C (Fig. S1b). These topographic images show a triangular (honeycomb) superlattice of bright (dark) areas, which are regions of twisted bilayer graphene that exhibit local AA (AB/BA) stacking[1–3]. In Fig. S1a, two different lattice scales can be seen: the graphene-hBN moiré lattice (1.76 nm moiré wavelength; 8° relative twist angle) and the graphene-graphene moiré lattice (13.3 nm moiré wavelength; 1.06° relative twist angle; 0.1% interlayer relative strain). In Fig. S1b, only the graphene moiré lattice can be seen (1.18° twisted bilayer graphene, 0.3% interlayer relative strain, no observable graphene/h-BN moiré pattern). Although C_3 symmetry is broken by the strain measured in these devices, C_2 symmetry does not appear to be broken in the moiré superlattice pattern. Similarly, Device B has a 1.04° graphene-graphene moiré pattern (with 0.4% strain) and a 2.4 nm graphene-hBN moiré pattern (5.8° twist angle). Since the graphene-hBN twist angles are measured to be larger than 5° for all of the devices studied, our MATBG samples are clearly not aligned with their hBN substrates (perfect alignment produces a ~14 nm moiré pattern). Device A is the same sample as “Device A” in Wong *et al*.[4]

B. High-resolution DT-STS at 200 mK and low magnetic fields

Fig. S2 shows differential conductance $dI/dV(V_s, V_g)$ obtained at the center of an AA site in Device A (which is the device from which data in main text Figs. 1 and 2 come from), measured at T = 205 mK at $B_\perp$ = 1 T (Fig. S2a) and $B_\perp$ = 3 T (Fig. S2b). Triangular markers in this figure mark the position of the strongly correlated Chern insulating states discussed in the

main text and observed at these field strengths at partial fillings of the conduction (Figs. S2a,b; red triangles) or valence (Figs. S2a,b; blue triangles) flat bands, with the number of left-pointing arrows identifying the absolute value of the Chern number of each gap. We observe a number of gaps in both the upper and lower flat bands, including two gaps near $\nu = +2$ (clearer in Fig. S2b) and $\nu = -2$ (clearer in Fig. S2a), which are very narrow in gate-range, and two gaps in the intervals $-3 < \nu < -2$ and $+2 < \nu < +3$ (marked by shaded boxes in Fig. S2). As mentioned in the main text, the gaps identified by shaded boxes in Fig. S2 do not systematically shift along the V_g axis with the application of a perpendicular magnetic field. Thus, they lie beyond the scope of this manuscript and will be discussed elsewhere.

Interestingly, the cascade of transitions seen at higher temperatures (T = 6 K in Ref. 4 and at higher magnetic fields (main text Fig. 1e) are much weaker at low temperature, low magnetic fields (Figs. S2a,b). This is reminiscent of transport on MATBG, which often show peaks in resistivity (most often at $|\nu| = 1$) diminish as the temperature is lowered[5–8]. More studies are needed to understand this strange phenomenon and to uncover the relationship between the flavor symmetry of MATBG and the system's temperature and magnetic field strength.

C. Higher-index Landau levels near charge neutrality

Fig. S3a shows differential conductance $dI/dV(V_s, V_g)$ obtained at the center of an AA site in Device B, measured at T = 320 mK in a $B_\perp$ = 2.3 T out-of-plane magnetic field. The two peak features in dI/dV that pass through the Fermi energy (E_F; V_s = 0 mV) between V_g = 16 V and V_g = 8 V are the eight zeroth Landau levels (ZLLs) discussed in the main text. In addition, at low magnetic fields, several quartets of higher-index Landau levels (LLs) can be seen crossing the Fermi energy for filling fractions $\nu_{LL} > 4$ ($V_g > 16$ V) and $\nu_{LL} < -4$ ($V_g < 8$ V), where $\nu_{LL} = n\Phi_0/B$ is the number of filled LLs at carrier density n and $\Phi_0 = h/e$ is the magnetic flux quantum. The higher-index LLs of the conduction flat band are only visible when the sample is n-doped ($V_g > 16$ V), and likewise for the LLs of the valence flat band when the sample is p-doped ($V_g < 8$ V).

Fig. S3b shows the same measurement of dI/dV divided by I/V_s, which is used to partially correct for changes in the initial tunneling feedback condition at different gate voltages V_g in systems where there are large variations in tunneling current I. In this plot, both the ZLLs and the higher-index LLs are more clearly discernible than in Fig. S3a. Seven spectroscopic gaps (Fig. S3a; marked by purple triangles) equally spaced in V_g are seen and are labeled by their LL filling ν_{LL} on the right side of Figs. S3a,b. We note that the large energetic separation between the ZLLs and the conduction (valence) band LLs in Fig. S3b for $\nu > 0$ ($\nu < 0$) is consistent with the sign-switching Haldane mass described in the main text[9,10].

While the quartets of the ZLLs are each seen to split into four, singly-degenerate LLs as a result of quantum Hall ferromagnetism[11–13], higher-index LLs are not seen to split at E_F (within our energy resolution). Instead, they pin to E_F over a carrier density range equal to $\Delta n = 4B/\Phi_0$. These density-tuned scanning tunneling microscopy (DT-STS) measurements are in agreement with those of magnetotransport experiments, which have identified a fourfold-degenerate LL fan emanating from charge neutrality[6,14,15].

D. Magnetic-field dependence of zeroth Landau Level quartet splitting

As discussed in the main text, $dI/dV(V_s, V_g)$ measurements show two peaks that represent two fourfold-degenerate zeroth LLs. These peaks are energetically separated by roughly 3 - 11 meV (depending on the magnetic field strength) when both fourfold-degenerate ZLLs are fully occupied or fully empty. This splitting, which could be caused by several possible single-particle effects (strain[16], orbital Zeeman effect[17–19], interlayer bias[20]), appears to increase roughly linearly with magnetic field (see Fig. S4). Theoretical calculations for orbital magnetism in MATBG[17] predict a large orbital Zeeman splitting corresponding to a g-factor on the order of 10, which is consistent with the data in Fig. S4. However, we cannot rule out the influence of heterostrain, which lifts the degeneracy of Dirac points at opposite corners of a moiré Brillouin zone[16,21].

E. Effects of local STM tip potential on spectroscopic gap measurements: charging energy and Coulomb diamonds

As noted in Xie *et al*.[22], the relationship between the gate voltage V_g and the density n may be affected by tip-induced band bending. In our experiment, we greatly reduce the influence of the tip by using a tungsten tip poked into copper (both tungsten and copper have work functions similar to graphene). Improvements in the surface cleanliness of the samples also reduce the influence of tip-induced band bending by decreasing the likelihood that the tip picks up contaminants that modify its work function. However, the effect of the tip cannot be completely eliminated. Tip-induced band bending contributes to the gate-voltage widths of the Chern gaps, increasing the size of the error bars in main text Fig. 3. We describe below how tip-induced band bending affects our measurements.

When performing STM measurements on two-dimensional gate-tunable systems, the STM tip is placed within a nanometer of the sample surface. Hence, the STM tip produces a local electrostatic potential $V(\boldsymbol{r})$ whose strength and profile depend on a number of characteristics of the tip, such as the work function and the tip shape (see Fig. S5a for a schematic). Because the band structure of MATBG varies greatly with carrier density, these local modulations in the chemical potential caused by the tip potential can greatly affect the local conductivity of the sample, presenting distinct challenges when performing spectroscopic studies within these samples.

Consider the situation where the filling factor ν in MATBG is tuned near that of a strongly correlated Chern insulating phase. Because of the narrow gate range associated with each Chern phase, it is possible for tip-gating effects to produce a local chemical potential distortion $\mu(r)$ where a ring-shaped region of MATBG is in the insulating phase, while a “quantum dot” region below the tip and the region far away from the tip remain conducting (Fig. S5c). If the insulating phase occurs at chemical potential μ_ν, the insulating ring occurs at radius r_ν, where $\mu(r = r_\nu) = \mu_\nu$. Regions $r > r_\nu$ and $r < r_\nu$ remain conducting. This situation is essentially a double-barrier tunneling junction consisting of the metallic tip, the conducting quantum dot, and the conducting outer region of the sample, sequentially separated by the insulating vacuum tunnel barrier and the insulating ring-shaped region. The size of the quantum dot (and thus the charging energy) is tunable via the back-gate because the back-gate shifts $\mu(r)$. In spectroscopy, we observe this effect as a string of Coulomb diamond features at E_F (Fig. S5d; marked by black triangles) and nearly horizontal charging lines (Fig. S5d; marked by blue triangles) that indicate the addition of a single electron to the quantum dot[23]. As the quantum dot

under the tip apex shrinks, the V_g-spacing of the charging lines increases because a larger change in density is required to add a single electron to the dot (i.e. the capacitance decreases, so ΔV_g between charging lines increases).

In Fig. S5d, the V_g-spacing between charging lines and Coulomb diamonds are generally larger for larger V_g (although not monotonically, possibly due to the single-particle energies of electrons in the dot). From this observation, we infer that the quantum dot and the insulating ring shrink with increasing V_g. Eventually, $r_\nu \to 0$, and the insulating region is directly under the tip apex. This would indicate that the spectroscopic Chern gap (i.e. the true gap in the LDOS) is located slightly above (between 0.1 V and 0.2 V along the V_g axis in Fig. S5d) these charging events.

F. Raw d*I*/d*V*(V_s,V_g) as a function of magnetic field for Devices B and C

Measurements in Fig. 1 and Fig. 2 of the main text were taken on Device A, which showed signatures of the complete sextet of field-induced correlated Chern insulating phases emanating as a function of magnetic field from every integer filling ν and the octet of ZLLs near charge neutrality. Figs. S6 and S7 depict representative data acquired from Device B and Device C, respectively, at a variety of magnetic field strengths. As explained in more detail in Supplementary Section G, these devices quantitatively reproduce the Chern numbers observed in Device A.

G. Quantized field response of strongly correlated Chern gaps in Devices B and C

Figs. S8a,b summarize our measurements on Devices B and C by plotting the gate voltage at which each gap in spectroscopy occurs with respect to a perpendicular magnetic field. As in Fig. 3a in the main text, the red (blue) points represent gaps seen away from the CNP within the conduction (valence) flat band, while purple points represent gaps between LLs near the CNP. Each point represents the center of a gap measured at E_F, where error bars were chosen to encapsulate the full gate range of each gap (error analysis as described in Supplementary Section J). The data obtained in Device B were acquired between 300 mK and 320 mK, and the data obtained in Device C were acquired at roughly 6.5 K.

In Device B (Fig. S8a), we identify field-induced strongly correlated Chern states with C = +3 emanating from ν = +1, C = +2 from ν = +2, and C = +1 from ν = +3. Additionally, we identify a single gap at 9 T consistent with a Chern state with C = -2 emanating from ν = -2, but we were unable to clearly identify this gap at other field strengths. In our measurements of this device, the valence flat band appears to be split into two peaks, and the Chern insulating gaps are not apparently present for ν < 0 (except C = -2 at 9 T). The cause for this is unclear, but could possibly be attributed to the non-negligible interlayer strain (ε = 0.4%) observed in this device. Theoretical studies have shown that even small amounts of strain can vastly affect the bandwidth of the flat bands in MATBG[16]. A significant increase in the effective bandwidth of the valence band may be responsible for the absence of nearly all signatures of correlation-induced Chern phases for ν < 0 in this device.

In Device C (Fig. S8b), we identify strongly correlated Chern states with C = ±2 emanating from ν = ±2 and C = ±1 from ν = ±3. In addition, we identify a single gap at 9 T consistent with the preformation of a Chern state with C = -3 from ν = -1. This gap is only partially formed, where the zero-bias conductance is seen to suppress within a small gate range

but is not observed to reach zero conductance. Additionally, this gap appears to induce kinks in all passive bands (those observed away from E_F), implying a jump in the chemical potential of the system at this filling. Unlike for Devices A and B, all measurements on Device C were performed at roughly 6.5 K. The data presented from Device C represents our only observation of Chern phases at this temperature. We speculate that the transition temperatures for the Chern phases vary with twist angle and strain. We also note that the size of an energy gap may not be directly related to the transition temperature, as is the case for the C = 1 phase in hBN-aligned samples, where the gap size (~30 K) is larger than the Curie temperature (~7 K)[24]. We were unable to obtain data on Device C at millikelvin temperatures.

It is clear that, when observed, the Chern numbers seen in Devices B and C agree with those found in Device A. This point is most salient in main text Fig. 3b, where reparametrizing B and V_g in terms of dimensionless quantities causes the gap data from all three devices to collapse onto a single plot.

H. Method used to reparametrize spectroscopic gap information as a function of filling and fluxes per unit cell

In Fig. 3b of the main text, we plot the spectroscopic gap information extracted from DT-STS measurements performed at several magnetic fields from three separate devices. Here we detail the method used for converting the gate voltage V_g and magnetic field B of a gap to its associated flat-band filling factor ν and magnetic flux per superlattice unit cell Φ/Φ_0. This can be done using the DT-STS data alone, since the data implicitly contains the device capacitances and the moiré unit cell areas. Device capacitances can also be estimated through the parallel plate model, and moiré unit cell areas can be measured directly via topographic images, giving us a way to verify our method. The method is detailed as follows:

1. Measure the gate voltage V_g of the gap of interest at magnetic field B.
2. At zero magnetic field, measure the gate voltages corresponding to ν = +4 and ν = -4, which we label V_+ and V_-. These voltages are easy to identify because, at these filling factors, the single-particle gaps between the flat bands and the remote bands are prominent and quickly cross E_F.
3. The filling factor of the gap is simply $\nu = 8(V_g - V_-)/(V_+ - V_-) - 4$.
4. At the highest available magnetic field B_{max} (we used 9 T), the field at which the ZLL gaps are most prominent, measure the gate voltages corresponding to LL filling factors ν_{LL} = +4 and ν_{LL} = -4 LL gaps, which we label V_{LL+} and V_{LL-}.
5. LLs have a Chern number of +1, so they can be used as a figurative “meter stick” for measuring the Chern numbers of other insulating gaps. The total number of states in a LL at some magnetic field is equal to the total number of magnetic flux quanta that pierce the entire sample at that field. This means that $(V_{LL+} - V_{LL-})/8$ is a measure of the number of flux quanta in the sample at magnetic field B_{max} (scaled by the sample-gate capacitance), while $(V_+ - V_-)/8$ is a measure of the number of moiré unit cells in the sample (also scaled by the sample-gate capacitance). Thus, we take the ratio of these two quantities to convert the magnetic field B at which a gap is observed to units of flux quanta per moiré unit cell $\Phi/\Phi_0 = (B/B_{max})(V_{LL+} - V_{LL-})/(V_+ - V_-)$.

With this straightforward conversion method, we find that the data from three devices, with different twist angles and amounts of interlayer strain, all collapse onto a single plot, as shown in Fig. 3b of the main text.

I. Least squares analysis for the Diophantine equation

By integrating Streda's formula, $dn/dB = eC/h$, the relationship between the charge carrier density n of an insulating system with Chern number C and the magnetic field B is given by $n = CBe/h + n_0\nu_0$, where $n_0 = 1/\Omega$ is the density for one electron per moiré superlattice unit cell area Ω, and ν_0 is the number of electrons per superlattice unit cell at zero magnetic field[25]. C and ν_0 are integers (except in special cases where they take fractional values, such as for the fractional quantum Hall effect[26]). Dividing by n_0 gives $\nu = C\Phi/\Phi_0 + \nu_0$, where $\nu = n/n_0$, $\Phi = B/n_0$, $\Phi_0 = h/e$.

We fit the data in main text Fig. 3b using weighted least squares regression. We require ν_0 to be an integer, so the least squares line $\nu' = C\Phi/\Phi_0$ (where $\nu' = \nu - \nu_0$) is constrained to pass through the origin (fits without this restriction yield the same Chern numbers with larger error bounds). Each squared residual in the linear regression was weighted by the error in ν' (calculated through the errors in the gate voltages in step 3 of Supplementary Section H). The values of C obtained through this method are:

$$C = -1.37 \pm 0.29 \text{ from } \nu_0 = -3$$
$$C = -2.13 \pm 0.32 \text{ from } \nu_0 = -2$$
$$C = -3.14 \pm 0.33 \text{ from } \nu_0 = -1$$
$$C = 3.16 \pm 0.27 \text{ from } \nu_0 = 1$$
$$C = 2.15 \pm 0.25 \text{ from } \nu_0 = 2$$
$$C = 1.09 \pm 0.24 \text{ from } \nu_0 = 3$$

These values are consistent with the claim in the main text: $C = -1$ from $\nu_0 = -3$, $C = -2$ from $\nu_0 = -2$, $C = -3$ from $\nu_0 = -1$, $C = 3$ from $\nu_0 = 1$, $C = 2$ from $\nu_0 = 2$, and $C = 1$ from $\nu_0 = 3$.

J. Spectroscopic gap location and error extraction

When performing high-resolution spectroscopy measurements on MATBG, spectral gaps in the system are convolved with charging effects due to the unavoidable influence of the STM tip (discussed in Supplementary Section E). This can make it difficult to identify the precise gate voltages at which gaps in spectroscopy occur. Therefore, it is crucial that our method for extracting the gate voltage of each Chern gap is robust against the systematic errors that may arise in the data analysis process. For this reason, we use very conservative error bounds on the reported gate locations of the gaps, which were determined using a set of three criteria discussed in this section. With these criteria, the error bars reported in the summary Landau fan diagrams in main text Fig. 3 and in Fig. S8 were chosen to display the full V_g ranges of the observed spectral gaps, which consist of the charging effects (Coulomb diamonds) and Chern gaps. Stricter error bounds are unnecessary for this study because we have used Streda's theorem to analyze the magnetic-field dependence of each correlation-induced gap, which has the advantage of vastly reducing the measurements' conclusions to only integer-valued linear slopes in *n* vs. *B* plots.

To demonstrate the error analysis method we have used, Figs. S9a-d show the same data depicted in Fig. 1d of the main text within a restricted energy range around E_F (from -20

meV to +20 meV) and in a different color scale that highlights the Chern gaps and LLs observed at B = 6 T in the conduction (Fig. S9a,b) and valence (Fig. S9c,d) flat bands. Figs. S10a-d show the same data depicted in Fig. 1e of the main text with a similarly restricted energy range (from –12 meV to +12 meV) and in a saturated color scale that highlights the gaps observed at B = 9 T. Similar procedures for extracting error bounds of Chern gaps were carried out on equivalent data sets acquired at other magnetic fields, and on Devices B and C.

Dashed lines in Figs. S9a-d and S10a-d bound the error reported in the gate voltage of each gap. Correlated Chern gaps were found to exhibit the following characteristic signatures: (1) Each gap occurs only at E_F without association with any single-particle gap features away from E_F. This signifies an origin based on electronic interaction effects. (2) Each gap showed a strong suppression of LDOS around E_F, many times showing characteristics of a hard gap (i.e. zero conductance within a finite energy window around E_F) between Chern sub-bands. (3) Each gap is accompanied by an abrupt jump in the dispersion of features in the spectra away from E_F. This signifies a sudden change in the chemical potential of the system at these fillings.

Throughout much of this measurement, a persistent suppression of the spectral weight is observed around E_F, which is not seen at lower magnetic fields. This has previously been observed in magnetic-field-dependent tunneling spectroscopy in other electronic systems, and were attributed to Coulomb gaps[27,28].

Since the ZLL gaps are used as a figurative "meter stick" for measuring the Chern numbers of the correlated gaps, we must accurately determine V_g for the ZLL gaps. An example of how this is done is shown in Figs. S9b,c,e. The full width of the gap is bounded by the gate voltages where a LL is seen to cross zero bias (i.e. where the gap closes). The data points in main text Fig. 3 are taken to be the centers of the gaps (i.e. the arithmetic means of the upper and lower bounds), with the error bars taken to be the full widths. In Supplementary Section H, V_g is converted to ν using the $\nu_{LL} = \pm 4$ gaps, minimizing the influence of this error.

K. Chern insulating states: Staggered potential mass vs. Haldane mass

The Dirac points that connect the conduction and valence flat bands in MATBG can be gapped by breaking the C_2T symmetry of the system, where C_2 is 2-fold rotation about the z-axis, and T is time-reversal (which we define as spinless here, namely, T only acts on the orbital wave function and does not reverse spin). Breaking this composite symmetry can be done by breaking either the C_2 symmetry or the T symmetry of MATBG, as we discuss below. One could break both C_2 and T symmetry, but we do not consider such cases.

When C_2 symmetry is either externally broken (e.g. by alignment with the hBN substrate) or spontaneously broken (possibly by electronic interactions), the A and B sublattices of the microscopic graphene lattice become effectively inequivalent, and the Dirac points gap with equal masses (equal signs and magnitudes) in the K and K' valleys. We write this staggered sublattice potential mass as $m(\eta, s) = m$ at valley η and spin s ($\eta = \pm 1$ for K and K', and $s = \uparrow, \downarrow$). Since the Dirac cones of the K and K' valleys have opposite helicities, the conduction and valence flat bands at valley η carry Chern number $+\eta$ and $-\eta$, respectively, independent of spin. As a result, the 4 conduction bands at valley and spin $(+\uparrow, +\downarrow, -\uparrow, -\downarrow)$ carry Chern numbers (+1,+1,-1,-1)*sgn(m), and the 4 valence bands carry Chern numbers (-1,-1,+1,+1)*sgn(m), respectively, as shown in Fig. S12a, where sgn(m) is the sign of the mass. If interactions further split the degeneracy of these flat bands, such that each Chern band is either fully occupied or

fully empty at integer fillings, the system can form insulating gaps with Chern numbers C = ±1, 0 or ±2, ±1 near integer fillings ν = ±3, ±2, ±1, respectively (states with positive □ depicted in Fig. S12a).

In contrast, when T symmetry is spontaneously broken (by an interaction-induced "mean-field" Haldane mass term), the Dirac points gap with opposite masses (opposite signs and equal magnitudes) in the K and K' valleys. We write this Haldane mass as $m(\eta, s) = \eta m$ at valley η and spin s. In this case, all the 4 conduction bands (of both valleys and both spins) carry a Chern number sgn(m), while all the valence bands carry a Chern number -sgn(m). Assume the Chern numbers of the valence bands have the same sign as νB for filling $\nu \neq 0$ (justified in Supplementary Section L), as shown in Fig. S12b. If interactions further split the degeneracy of these bands (as in quantum Hall ferromagnetism), such that each Chern band is either fully occupied or fully empty at integer fillings, the system will form insulating gaps with Chern numbers C = ±1, ±2, ±3 near integer fillings ν = ±3, ±2, ±1, respectively (states at positive fillings depicted in Fig. S12b), as observed in our experiments.

L. Free energy argument for the extremal Chern number phases

As described in the main text, interactions in MATBG induce a Haldane mass term, which gaps the Dirac points that connect the conductance and valence flat bands to produce Chern bands with Chern numbers +1 or -1. Although we experimentally observe only one Chern phase near each integer filling, there are four choices for an interaction-induced mass term in MATBG (staggered potential mass or Haldane mass, each of which can be either positive or negative). At zero magnetic field, since the mass term does not couple the two valleys, the sign of the mass in each valley can be chosen freely. Thus, there is no reason to suspect that any of these 4 possible mass terms will be dominant, and hence their corresponding Chern phases will be degenerate at the mean-field level. Zero-magnetic-field transport measurements of MATBG unaligned with hBN do not show Chern insulating phases, implying either that these mass interactions could be sub-dominant to those driving correlated insulating or superconducting behavior or that the system could be broken into domains of different Chern numbers. However, we argue here that a small magnetic field can modify the free energies of the different possible Chern phases, favoring the Chern phase with the maximal Chern number that matches the sign of the filling factor ν times the magnetic field B of that state.

We assume an on-site (moiré site) Hubbard interaction U at zero magnetic field (see Supplementary Section M). We first consider the energy of the Chern phases with a negative Haldane mass term $m < 0$ (yielding mass ηm in valley η), which gives Chern numbers C = +1, +2, +3, +4, +3, +2, +1 at fillings ν = -3, -2, -1, 0, 1, 2, 3, respectively. In this case, all four conduction (valence) flat bands carry Chern number -1 (+1) (Fig. S13a). As shown by the zero-field analysis of Ref. 4, in the flat band limit, the chemical potential μ approximately jumps by U at each integer filling $\nu = \pm 1, \pm 2, \pm 3$, and jumps by $U + 2E_0$ at filling $\nu = 0$ (Fig. S13b; gray curve), where we have assumed the single-particle energies of the four conduction flat bands and four valence flat bands are at $\pm E_0$, respectively (in reality, these bands are coupled at zero energy by Dirac nodes, but we can capture the essential physics with this perfectly flat band approximation). In the presence of a Haldane mass, these jumps occur at the same fillings as the Chern insulator states we mentioned above. We choose $\mu = 0$ as the chemical potential of

the ungated MATBG at charge neutrality and zero magnetic field. Accordingly, the energy per moiré unit cell of the state at filling ν is given by

$$E(\nu) = \int_0^{\nu} \mu(\nu')d\nu' .$$

This is the energy required to adiabatically dope MATBG from charge neutrality to a filling ν state using the device's back-gate. At zero magnetic field, the chemical potential (Fig. S13b; gray curve) can be integrated to yield the energy $E(\nu)$, as shown by the gray curve in Fig. S13c.

We now consider the system at some small magnetic field $B > 0$ in dimensionless units of Φ/Φ_0 (for which the Landau levels are not yet well-developed). According to Streda's theorem, the number of electron states per moiré unit cell in each conduction (valence) flat band is given by 1 - B (1 + B), since the band has Chern number -1 (+1)[25]. For small B, we assume the interaction U is approximately unaffected by B, then the chemical potential μ as a function of the filling ν would become the red line of Fig. S13b, where μ jumps by U at fillings ν = -3 + B, -2 + 2B, -1 + 3B, 4B, 1 + 3B, 2 + 2B, 3 + B, respectively. These fillings are where the Chern insulator states occur under a negative Haldane mass. As a result, the chemical potential (Fig. S13b; red curve) integrates to yield an energy $E(\nu)$, shown by the red curve in Fig. S13c. In particular, for $B > 0$, the Chern number C = +3, +2, +1 insulators at positive fillings ν = 1 + 3B, 2 + 2B, 3 + B are all lower in energy compared to the (metallic) states expected at $B = 0$ at the same fillings. In contrast, still for $B > 0$, the Chern number C = +3, +2, +1 insulators at negative fillings ν = -1 + 3B, -2 + 2B, -3 + B are all higher in energy compared to the (metallic) states at $B = 0$ at the same fillings.

Under the same analysis for a positive Haldane mass term, we expect Chern numbers C = -1, -2, -3, -4, -3, -2, -1 at fillings ν = -3 - B, -2 - 2B, -1 - 3B, -4B, 1 - 3B, 2 - 2B, 3 - B, respectively. At $B > 0$, the chemical potential μ and associated energy $E(\nu)$ as functions of filling ν are illustrated by the blue curves in Figs. S13b,c, respectively. Furthermore, the same analysis can be done for the staggered potential mass term (present in hBN-aligned samples), which gives Chern numbers C = ±1, ±2 / 0, ±1, 0, ±1, ±2 / 0, ±1 at fillings ν = -3 ± B, -2 ± (2B / 0), -1 ± B, 0, 1 ± B, 2 ± (2B / 0), 3 ± B. In each case, one could obtain an energy curve by integrating the chemical potential.

One illustrative way to see that the Haldane mass term with the opposite sign as νB will form states with the lowest energy is to split the integral for $E(\nu)$ into two parts. Without loss of generality, we focus on positive fillings $\nu > 0$. We rely on the fact that all sequences of Chern states under a staggered potential mass term contain a C = 0 states at $\nu = 0$; whereas, for $\nu > 0$, the negative Haldane mass term admits a C = +4 state near $\nu = 0$. Thus, for fillings $0 < \nu < 4B$, $E(\nu) = \int_0^{\nu} \mu(\nu')d\nu'$ is negative if and only if the system has a negative Haldane mass term. For all systems in the presence of any staggered potential mass term, $E(\nu) = \int_0^{\nu} \mu(\nu')d\nu'$ is positive, and is thus unfavorable. For fillings $4B < \nu < 4$, we write the integral in two terms: $E(\nu) = \int_0^{4B} \mu(\nu')d\nu' + \int_{4B}^{\nu} \mu(\nu')d\nu'$. For the negative Haldane mass system, the first term is negative and the second term is always equal to or smaller than the second term of an analogous equation describing the energy of any staggered potential mass system. A nearly identical argument for negative filling $\nu < 0$ can be made.

By comparing the energies of various states due to different mass terms, at the same filling, it is then clear that for $B > 0$, a negative Haldane mass term yields the lowest energies at

positive filling $\nu > 0$, which yields insulators with Chern numbers C = +3, +2, +1 at fillings ν = 1 + 3B, 2 + 2B, 3 + B, respectively. On the other hand, a positive Haldane mass term yields the lowest energies at negative filling $\nu < 0$, which yields insulators with Chern numbers C = -3, -2, -1 at fillings ν = -1 - 3B, -2 - 2B, -3 - B, respectively. Therefore, we find the system favors a Haldane mass term of the opposite sign as νB when $B \neq 0$, yielding Chern states with maximal Chern numbers.

This is consistent with our observations of Chern number C = ±1, ±2, ±3 gaps near integer fillings ν = ±3, ±2, ±1, respectively. In principle, higher order energy considerations beyond the above simple argument may allow several Chern phases of different Chern numbers C to occur near a nonzero integer filling $\nu = \nu_i$ (each as a result of a different mass term that may become dominant at slightly different fillings $\nu = \nu_i + CB$), but thus far, we have found no experimental signatures for multiple Chern phases near any nonzero integer filling ν. However, future experiments on hBN-aligned devices (where C_2- and T-symmetry would both be broken) could uncover the coexistence of multiple sequences of Chern phases or a transition between the sequences as *B* is increased.

M. Phenomenological model of DT-STS data at high magnetic fields

As described in the main text, we postulate that our observations can be explained by a Haldane mass term that changes sign across the CNP (see Supplementary Section L for theoretical argument). A sign-switching Haldane mass implies (1) the appearance of Chern flat bands at zero magnetic field, and (2) ZLLs near filling $\nu = 0$ at finite magnetic fields large enough to develop clear LLs (the latter will be discussed later in this section). Here, we have defined the ZLLs to be those of massive Dirac fermions in the presence of a Haldane mass, which emerge no longer from zero energy, but from the band edge of the Chern +1 band. We observe that these ZLLs shift with carrier density, carrying states with Berry curvature from the conduction flat band to the valence flat band as the system is tuned between different topological ground states by increasing V_g (see Fig. S3 and main text Fig. 2a).

In this section, we provide a phenomenological model that assumes the existence of the Hofstadter Chern sub-bands and ZLLs, and includes mean-field interactions between electrons in those sub-bands and ZLLs, which we use to understand the LDOS measured away from E_F and use to extract quantitative measurements of the interaction strengths among these states. Our simple local interacting model describes the spectroscopic behavior of the flat sub-bands observed in DT-STS at finite magnetic field and correctly produces the density-dependent asymmetric ZLLs. Because the ZLLs only come from the edge of the Chern +1 sub-bands, this asymmetry cannot arise from a staggered sublattice potential mass term (i.e. the C_2-symmetry breaking mass from hBN alignment), which would produce symmetric ZLLs arising from Chern +1 sub-bands in both the conduction and valence flat bands. Instead, the asymmetric ZLL behavior can be explained by a Haldane mass, which only produces Chern +1 sub-bands in either the conduction or valence flat band and switches signs as the ZLLs move from the conduction flat band to the valence flat band. At zero magnetic field, electrons in MATBG localize to AA sites, thus setting the moiré wavelength λ_m as the natural length scale for Coulomb interactions, and in turn setting the natural energy scale for the Coulomb interaction to be on the order of 20 meV. Previous experiments have reported that the flat bands of MATBG split into a series of reduced degeneracy sub-bands as a result of this on-site Coulomb

(Hubbard) interaction U, where the energy of the splitting provided a direct measurement of $U = 23 \pm 5$ meV[4,29].

At a finite magnetic field *B*, the two Dirac points of the two flat bands at each spin and valley produce two ZLLs around zero energy. Each ZLL carries a Chern number C = +1. The energy states above (below) the two ZLLs are separated from the ZLLs by a large gap (gap size around $W\sqrt{B}$ where W is the bandwidth, $B = \Phi/\Phi_0$ is the magnetic field in units of flux per moiré unit cell), because the gap between the ZLLs and the first LLs of a Dirac fermion is the largest (the energy of the Nth LL in a Dirac system is $E(N) \propto \sqrt{N}$). Meanwhile, the energy states above (below) the ZLLs in each spin and valley are relatively close in energy (within an energy range $W(1-\sqrt{B})$ approximately), and carry a total Chern number C = -1, which we will regard as a Chern -1 sub-band. Therefore, for 2 spins and 2 valleys in total, we approximately regard the system (at finite magnetic field and without interactions) as carrying 8 ZLLs with Chern number C = +1 at zero energy, and 4 upper (lower) Chern sub-bands with Chern number C = -1. In real space, states are localized on the magnetic length scale. At a magnetic field corresponding to $\frac{p}{q}$ fluxes per moiré unit cell ($B/n_0 = \frac{p}{q}\Phi_0$), where p and q are coprime integers and $0 < \frac{p}{q} < 1$, according to the Streda formula, p ZLL electron states in each ZLL band and $q - p$ Chern sub-band states in each Chern sub-band are localized within a cluster of q AA sites, which make up a single magnetic unit cell.

We assume that interaction energies are much larger than the bandwidths of the ZLLs and of the upper (lower) Chern sub-bands. We then assume that within a cluster of q moiré unit cells (i.e. a magnetic unit cell), there are two groups of (q - p) spin-valley 4-fold degenerate Chern sub-band orbitals that make up the upper and lower Chern sub-bands. Within each of these groups, the q-site magnetic unit cell is evenly distributed among these (q – p) states, where each of these orbitals occupies an area of q / (q - p) moiré unit cells (i.e. non-overlapping within each group). Similarly, there are 2p spin-valley 4-fold degenerate ZLL orbitals, each of which occupies an area of q/p moiré unit cells (non-overlapping within each group). The Hamiltonian within the q moiré unit cells is the following:

$$H = H_0 + \frac{1}{2}\sum_{\alpha,\beta=C_C,C_v,Z} U_{\alpha\beta}\sum_{i=1}^{N_\alpha}\sum_{j=1}^{N_\beta}\lambda_{i,\alpha}^{j,\beta}\left(n_{i,\alpha}-\frac{1}{2}\right)\left(n_{j,\beta}-\frac{1}{2}\right),$$

$$H_0 = E_+\sum_{i=1}^{4(q-p)}\left(n_{i,C_C}-n_{i,C_V}\right) + E_0\sum_{i=1}^{4p}\left(n_{i,Z_1}-n_{i,Z_2}\right)$$

where C_C, C_V, Z_1, Z_2 stand for the upper Chern sub-bands, the lower Chern-sub-bands, and the ZLLs at single-particle energies E_0 and $-E_0$, respectively, $N_{C_C} = N_{C_V} = 4(q-p)$ and $N_{Z_i} = 4p$ are the number of states of the three kinds of sub-bands within the cluster of q AA sites, E_+ and E_0 are the single-particle energies of the upper 4 Chern sub-bands and the upper 4 ZLLs, and $n_{i,\alpha}$ =0 or 1 is the electron occupation number of state i in band α. The interaction $U_{\alpha\beta}$ is a symmetric matrix with matrix elements given by three numbers $U_{C_CC_C} = U_{C_CC_V} = U_{C_VC_V} = U_{CC}$, $U_{Z_iC_C} = U_{Z_iC_V} = U_{ZC}$ and $U_{Z_iZ_j} = U_{ZZ}$. They represent the local interactions within the 8 Chern sub-bands with Chern number -1, between the Chern sub-bands and the ZLLs, and within the ZLLs, respectively. $\lambda_{i,\alpha}^{j,\beta}$ is a dimensionless factor defined as the overlapping area of orbitals

(i,α) and (j,β) divided by the smaller of the areas of orbitals (i,α) and (j,β). Therefore, $0 \leq \lambda_{i,\alpha}^{j,\beta} \leq 1$ characterizes how close to each other the two orbitals (i,α) and (j,β) are. Note that this is a classical model (without non-commuting terms). The model is intuitively illustrated in Fig. S14a. We then calculate the spectral weight of this model at different fillings using the classical Monte Carlo method.

The spectroscopic features in DT-STS data measured emanating from near every strongly correlated Chern insulating gap first emerge at E_F and extend to roughly ±20 meV before vanishing, which qualitatively parallel previously reported cascade of features in zero magnetic field[4]. The spectroscopic behavior of the cascade features at zero magnetic field were attributed to the on-site localization of electrons and allowed us to measure the Coulomb repulsion energy. Here, in the presence of a magnetic field, we can perform a similar analysis on the cascade features emanating from sequential Chern sub-band splittings (main text Fig. 1e; $V_g \in [-39V, -10.9V] \cup [13.8V, 42V]$) and from sequential ZLL quantum Hall ferromagnetic splittings (main text Fig. 1e; $V_g \in [-10.9V, 13.8V]$), where the magnitudes of the sub-band or ZLL splittings can approximately give the intraband interactions between electrons within Chern sub-bands (U_{CC}) and ZLLs (U_{ZZ}), respectively. These splittings strongly resemble the splitting of spin-degenerate bands into Hubbard sub-bands in the Hubbard model, where the splitting is equal to the on-site Hubbard interaction.

Additionally, we observe the ZLLs to disperse in energy as a function of filling ν (main text Fig. 1e, $V_g \in [-39V, -10.9V] \cup [13.8V, 42V]$) while the Chern sub-bands are pinned to E_F. This is the result of interband interaction U_{ZC} between electrons in Chern sub-band states and ZLL states, which can be understood at the mean-field level as follows. Without loss of generality, assume the lower Chern sub-bands are partially filled, while the upper Chern sub-bands and the ZLLs are all fully unoccupied, namely, $n_{i,C_V} = n_{i,Z_1} = n_{i,Z_2} = 0$. In this case, the average occupation of the lower Chern sub-band orbital is $\langle n_{i,C_V} \rangle = \left(\frac{\nu}{4} + 1\right)\frac{q}{q-p}$, where ν is the filling fraction of the original moiré unit cell. By the definition of our Hamiltonian H, adding an electron in the lower Chern sub-bands cost an average energy equal to the chemical potential $\mu(\nu) = \frac{\partial H}{\partial n_{i,C_V}}$ at filling ν. At the same time, adding an electron in the lower 4 ZLLs cost an energy $\frac{\partial H}{\partial n_{i,Z_2}}$. Therefore, one expects to observe the lower ZLL spectral weight peak at energy bias $E_{Z_2}(\nu) \approx \frac{\partial H}{\partial n_{i,Z_2}} - \mu(\nu) = \frac{\partial H}{\partial n_{i,Z_2}} - \frac{\partial H}{\partial n_{i,C_V}}$. We can then calculate the slope of this peak with respect to filling ν, which is (for $p/q < 1/2$)

$$\frac{\partial E_{Z_2}(\nu)}{\partial \nu} = \frac{\partial}{\partial \nu}\left(\frac{\partial H}{\partial n_{i,Z_2}} - \frac{\partial H}{\partial n_{i,C_V}}\right) \approx \frac{q}{4(q-p)}\sum_j \frac{\partial}{\partial n_{j,C_V}}\left(\frac{\partial H}{\partial n_{i,Z_2}} - \frac{\partial H}{\partial n_{i,C_V}}\right)$$
$$= \frac{q}{p}U_{CZ} - \frac{q}{q-p}U_{CC},$$

where we have used the fact that $\sum_j \lambda_{i,Z_2}^{j,C_V} = 4\frac{q-p}{p}$ for $p/q < 1/2$. This is expected to be the average slope of the lower ZLL peak vs. ν in this regime (which corresponds to $V_g \in$

$[-39V, -10.9V]$ in main text Fig. 1e). One can show the higher ZLL peak has the same slope in this regime. Ultimately, given U_{CC}, this allows us to extract out U_{CZ}.

We consider the data from Device A at *B* = 9 T (main text Fig. 1e), where all three interaction measurement signatures are clearly visible (i.e. the Chern sub-band splittings, the ZLL splittings, and the energy dispersion of the fully filled/empty ZLLs as a function of filling). From the direct observation of the maximum energy to which the Chern sub-bands extend, we estimate the interaction strength between Chern sub-bands at this field strength to be $U_{CC} = 17 \pm 3$ meV, a value slightly smaller than the zero-field equivalent (i.e. the on-site Hubbard interaction *U*). One expects this inequality $U_{CC} < U$ from the intuitive understanding that the localization of states of a single band at zero field (one state per AA sites) is slightly stronger than that of a Chern sub-band at finite magnetic field (two states per three AA sites at ~9 T), purely resulting from the Hofstadter criterion.

Similarly, using the direct observation of the maximum energy to which the ZLLs extend, we estimate the interaction strength between ZLLs at this field to be $U_{ZZ} = 7 \pm 1.5$ meV. This energy is far smaller than U_{CC} at this field strength because each local orbital in these LLs is delocalized to roughly three AA sites, allowing for significantly less overlap between wavefunctions.

Finally, the dispersion slope of the ZLLs was measured in the upper gate regime ($V_g \in [13.8V, 42V]$) of main text Fig. 1e, where the ZLLs are seen to increase in energy by 10.9 meV over the full filling of the 4 upper Chern bands, each with filling $(1 - p/q)\Phi/\Phi_0 = (1 - 0.304)\Phi/\Phi_0$, where $0.304\Phi/\Phi_0$ is equivalent to 9 T in Device A. Thus, we measure the slope to be this energy divided by the total ν: $\frac{\Delta E_{Z+}}{\Delta \nu} = 10.9\, meV/4(1 - 0.304\ \Phi/\Phi_0)$. This slope was explained to be equal to $\frac{q}{p}U_{CZ} - \frac{q}{q-p}U_{CC}$ above. Thus, we extract a value for the interband interactions between the ZLL states and Chern band states to be $U_{ZC} = 8.5 \pm 1.5$ meV from this measurement. This value is smaller than U_{CC}, but larger than U_{ZZ}, explained by the intermediate level of wavefunction overlap between the slightly delocalized Chern sub-band orbitals and the greatly delocalized ZLL orbitals at B = 9 T.

The numerical results (calculated by Monte Carlo method) of the spectral weight for this interaction model, using the experimentally extracted parameters above, are shown in Fig. S14b (Simulation parameters: $B/n_0 = \frac{3}{8}\Phi_0$, $U_{CC} = 15.6$ meV, $U_{CZ} = 7.6$ meV, $U_{ZZ} = 7.4$ meV, $E_+ = 14$ meV, $E_0 = 5$ meV). The Monte Carlo calculation for the quantum dot model with 8q orbitals in the q moiré unit cells is done using the Metropolis algorithm[30] as follows (which is generically used in the Ising model). For notation convenience, we sort the 8q orbitals in the q moiré unit cells (which are labeled by (i, α) in the above quantum dot Hamiltonian H) in a certain fixed order, and denote the occupation number of the k-th orbital as n_k $(1 \le k \le 8q)$. The Monte Carlo is done at a fixed temperature T and a given chemical potential μ. In the first step, we start from a random configuration of occupation numbers $n_k = 0$ or 1, where k runs over all the 8q orbitals. We denote this initial occupation configuration as $\{n_k^{(1)}\}$, and denote the total energy of this initial configuration (defined as $H - \mu \sum_k n_k$) as $E_{tot}^{(1)}$. Then, in the m-th step ($m \ge 2$), we flip the occupation number of the k_m-th orbital from $n_{k_m}^{(m-1)}$ to $1 - n_{k_m}^{(m-1)}$, where $k_m = m\ (mod\ 8q) + 1$, and examine the increment of the total energy $\Delta E^{(m)}$ after the occupation number flip. By

defining a flipping probability $p_m = \min(1, e^{-\Delta E^{(m)}/k_B T})$, we keep the flip (i.e., define the configuration of the m-th step as $n_k^{(m)} = n_k^{(m-1)}$ for $k \neq k_m$, and $n_{k_m}^{(m)} = 1 - n_{k_m}^{(m-1)}$) with probability p_m, and reverse the flip (i.e. define $n_k^{(m)} = n_k^{(m-1)}$ for all k) with probability $1 - p_m$. The total energy (the value of $H - \mu \sum_k n_k$) of the configuration $\left\{n_k^{(m)}\right\}$ in the m-th step is denoted by $E_{tot}^{(m)}$. After sufficient number of steps, the configurations will converge into those at low energies according to the probabilities given by the partition function. The convergence is slower for lower temperatures T. If the number of steps in total is N_{MC}, the spectral weight at energy ω can be calculated by

$$A(\omega) = \frac{1}{N_{MC} - N_0} \sum_{m=N_0}^{N_{MC}} \sum_{k=1}^{8q} Im\left(\frac{1}{\omega + i\delta - (-1)^{n_k^{(m)}} \left(E_k^{(m)} - E_{tot}^{(m)}\right)} \right),$$

where N_0 is a step number after which the configurations are trusted to be distributed according to the partition function, δ is a small positive number for smearing out the delta functions numerically, and $E_k^{(m)}$ is the value of $H - \mu \sum_k n_k$ for the occupation configuration with $n_{k'} = n_{k'}^{(m)}$ for $k' \neq k$ and $n_k = 1 - n_k^{(m)}$. The filling fraction per moiré unit cell is given by

$$\nu = \frac{1}{q(N_{MC} - N_0)} \sum_{m=N_0}^{N_{MC}} \sum_{k=1}^{8q} \left(n_k^{(m)} - \frac{1}{2}\right).$$

In our calculations, we take a temperature T = 6 K (higher than the experimental temperature, for numerical convergence), $N_{MC} = 2000$, $N_0 = 400$, and 1000 values of chemical potential μ are examined.

This calculation qualitatively reproduces the spectroscopic features measured in Fig. 1e of the main text. For filling factor $|\nu| > 3/2$, our calculations show the sequential splitting of the Chern sub-bands that make up the conduction and valence flat bands. For filling factor $|\nu| < 3/2$, our calculations show the sequential splitting and degeneracy liftings of the ZLLs as a result of quantum Hall ferromagnetism. Fig. S14c shows line cuts of Fig. S14b, which highlights the asymmetry in the ZLLs when MATBG is n-doped vs. when it is p-doped. This agrees with the direction of the ZLL energy shifting under a Haldane mass term of the opposite sign as νB. Because the Chern numbers and degeneracies of each band in this model have been defined by hand, this model is phenomenological and cannot explain the mechanism that gives rise to the mean-field Haldane mass or the strongly correlated Chern gaps. However, it does connect the features of the spectroscopic data to the existence of the Chern sub-bands and the ZLLs.

N. Quantum Hall ferromagnetism in the zeroth Landau level

We interpret the 9 gaps near the CNP in main text Fig. 2a as quantum Hall ferromagnetic states due to electron-electron-interaction driven breaking of the symmetry of the zeroth Landau level. This is consistent with the observation that the gaps are evenly spaced in gate voltage by an amount compatible with a parallel-plate capacitance model ($\frac{\Delta \nu_{LL} e^2 B}{h} = \frac{\epsilon}{d} \Delta V_g$, where $\epsilon \approx 4\epsilon_0$ and $d \approx 300$ nm). This is also consistent with transport measurements, which observe the lifting of the degeneracy of the CNP Landau fan at similar magnetic fields[6,14,15]. This stands in contrast to Jung *et al*.[28], where O(10 meV)-wide Coulomb diamonds are observed

when the ZLL crosses E_F due to localization of states in an electron-hole puddle. In MATBG, the energy scale of the splitting of the ZLLs is ~8 meV, which is smaller than the Coulomb blockade energy for tunneling into an AA-site quantum dot (~20 meV). Furthermore, the gaps in main text Fig. 2a lack a diamond shape, but instead the gaps run parallel to the V_g-axis for some ranges of the gate voltage.

References:

1. Li, G. *et al.* Observation of Van Hove singularities in twisted graphene layers. *Nat. Phys.* **6**, 109–113 (2010).
2. Brihuega, I. *et al.* Unraveling the intrinsic and robust nature of van hove singularities in twisted bilayer graphene by scanning tunneling microscopy and theoretical analysis. *Phys. Rev. Lett.* **109**, 196802 (2012).
3. Wong, D. *et al.* Local spectroscopy of moiré-induced electronic structure in gate-tunable twisted bilayer graphene. *Phys. Rev. B* **92**, 155409 (2015).
4. Wong, D. *et al.* Cascade of electronic transitions in magic-angle twisted bilayer graphene. *Nature* **582**, 198–202 (2020).
5. Polshyn, H. *et al.* Large linear-in-temperature resistivity in twisted bilayer graphene. *Nature Physics* vol. 15 1011–1016 (2019).
6. Lu, X. *et al.* Superconductors, orbital magnets and correlated states in magic-angle bilayer graphene. *Nature* **574**, 653–657 (2019).
7. Cao, Y. *et al.* Nematicity and Competing Orders in Superconducting Magic-Angle Graphene. (2020).
8. Saito, Y. *et al.* Isospin Pomeranchuk effect and the entropy of collective excitations in twisted bilayer graphene. *arXiv:2008.10830* (2020).
9. Haldane, F. D. M. Model for a quantum hall effect without landau levels: Condensed-matter realization of the 'parity anomaly'. *Phys. Rev. Lett.* **61**, 2015–2018 (1988).
10. Okada, Y. *et al.* Observation of dirac node formation and mass acquisition in a topological crystalline insulator. *Science* **341**, 1496–1499 (2013).
11. Nomura, K. & MacDonald, A. H. Quantum Hall ferromagnetism in graphene. *Phys. Rev. Lett.* **96**, 256602 (2006).
12. Young, A. F. *et al.* Spin and valley quantum Hall ferromagnetism in graphene. *Nat. Phys.* **8**, 550–556 (2012).
13. Song, Y. J. *et al.* High-resolution tunnelling spectroscopy of a graphene quartet. *Nature* **467**, 185–189 (2010).
14. Cao, Y. *et al.* Unconventional superconductivity in magic-angle graphene superlattices. *Nature* **556**, 43–50 (2018).
15. Yankowitz, M. *et al.* Tuning superconductivity in twisted bilayer graphene. *Science* **363**, 1059–1064 (2019).
16. Bi, Z., Yuan, N. F. Q. & Fu, L. Designing flat bands by strain. *Phys. Rev. B* **100**, 035448 (2019).
17. Bultinck, N., Chatterjee, S. & Zaletel, M. P. Mechanism for Anomalous Hall Ferromagnetism in Twisted Bilayer Graphene. *Phys. Rev. Lett.* **124**, 166601 (2020).
18. Zhang, Y.-H., Mao, D. & Senthil, T. Twisted Bilayer Graphene Aligned with Hexagonal Boron Nitride: Anomalous Hall Effect and a Lattice Model. *Phys. Rev. Res.* **1**, (2019).
19. Liu, J. & Dai, X. Theories for the correlated insulating states and quantum anomalous Hall phenomena in twisted bilayer graphene. *arXiv:1911.03760* (2019).
20. Moon, P., Son, Y. W. & Koshino, M. Optical absorption of twisted bilayer graphene with interlayer potential asymmetry. *Phys. Rev. B* **90**, 155427 (2014).
21. Po, H. C., Zou, L., Vishwanath, A. & Senthil, T. Origin of Mott Insulating Behavior and

Superconductivity in Twisted Bilayer Graphene. *Phys. Rev. X* **8**, 031089 (2018).
22. Xie, Y. *et al.* Spectroscopic signatures of many-body correlations in magic-angle twisted bilayer graphene. *Nature* **572**, 101–105 (2019).
23. Velasco, J. *et al.* Visualization and Control of Single-Electron Charging in Bilayer Graphene Quantum Dots. *Nano Lett.* **18**, 5104–5110 (2018).
24. Serlin, M. *et al.* Intrinsic quantized anomalous Hall effect in a moiré heterostructure. *Science* **367**, 900–903 (2020).
25. Středa, P. Theory of quantised Hall conductivity in two dimensions. *J. Phys. C Solid State Phys.* **15**, L717 (1982).
26. Spanton, E. M. *et al.* Observation of fractional Chern insulators in a van der Waals heterostructure. *Science* **360**, 62–66 (2018).
27. Morgenstern, M., Haude, D., Klijn, J. & Wiesendanger, R. Coulomb pseudogap caused by partial localization of a three-dimensional electron system in the extreme quantum limit. *Phys. Rev. B* **66**, 1–4 (2002).
28. Jung, S. *et al.* Evolution of microscopic localization in graphene in a magnetic field from scattering resonances to quantum dots. *Nat. Phys.* **7**, 245–251 (2011).
29. Zondiner, U. *et al.* Cascade of phase transitions and Dirac revivals in magic-angle graphene. *Nature* **582**, 203–208 (2020).
30. Metropolis, N., Rosenbluth, A. W., Rosenbluth, M. N., Teller, A. H. & Teller, E. Equation of state calculations by fast computing machines. *J. Chem. Phys.* **21**, 1087–1092 (1953).

SUPPLEMENTARY FIGURE S1

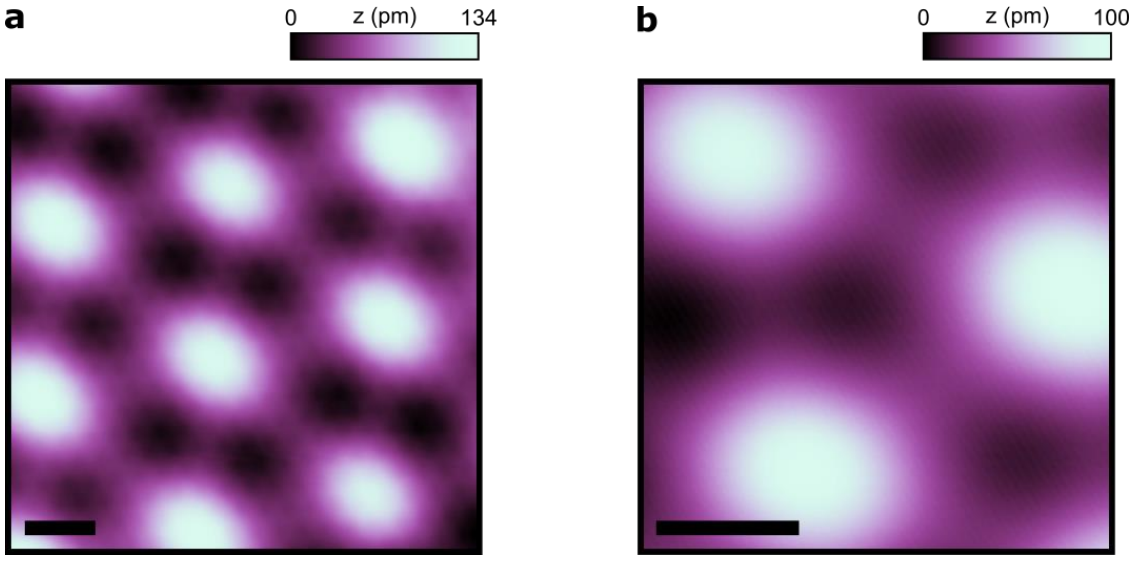

Figure S1 | STM topographic identification of hBN-graphene lattice misalignment. a, STM topographic image of 1.06° MATBG (Device A) with a visible hBN-graphene moiré pattern (V_S = -98 mV, I = 200 pA; Scale bar = 5 nm). **b,** STM topographic image of 1.18° MATBG (Device C) without a visible hBN-graphene moiré pattern (V_S = -150 mV, I = 200 pA; Scale bar = 5 nm).

SUPPLEMENTARY FIGURE S2

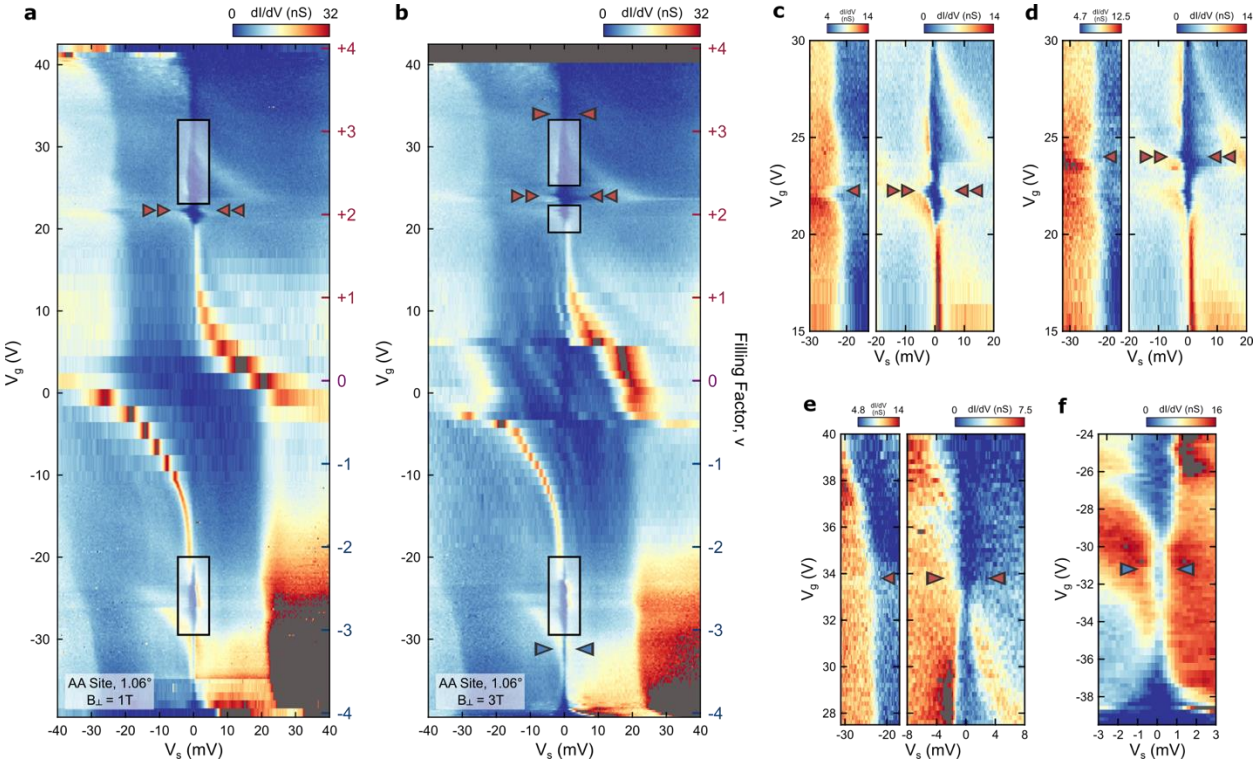

Figure S2 | Magnetic-field independent spectroscopic gaps in MATBG at T = 200 mK. a, d*I*/d*V*(V_s,V_g) measured at the center of an AA site in Device A at B = 1 T. **b,** d*I*/d*V*(V_s,V_g) measured at the center of an AA site in Device A at B = 3 T. Features near E_F in **b** between -1 < ν < 1 may be ZLLs and higher-index LLs. Shaded boxes indicate gaps that appear not to move along the V_g axis with increasing magnetic field. Arrows identify strongly correlated Chern insulating gaps near fillings +3, +2, and -3, with Chern numbers +1, +2, and -1 respectively, that move along the V_g axis with increasing magnetic field. (Initial tunneling parameters: V_s = -80 mV (**a**,**b**); I = 1.5 nA (**a**,**b**); 4.121 kHz sinusoidal modulation at V_{rms} = 200 μV (**a**,**b**)). **c,** Same d*I*/d*V*(V_s,V_g) data as **a** in a saturated color scale used to highlight a strongly correlated Chern gap near filling +2 with Chern number +2 gap. **d,e,f,** Same d*I*/d*V*(V_s,V_g) data as **b** in saturated color scales used to highlight strongly correlated Chern gaps near fillings +3 (**d**), +2 (**e**), and –3 (**f**), with Chern numbers +1 (**d**), +2 (**e**), and –1 (**f**), respectively. A nearby band edge is also shown for **c**, **d**, and **e**, which each shows a sudden shift in the energy of the band that signals a change in the chemical potential commensurate with the gap opening.

SUPPLEMENTARY FIGURE S3

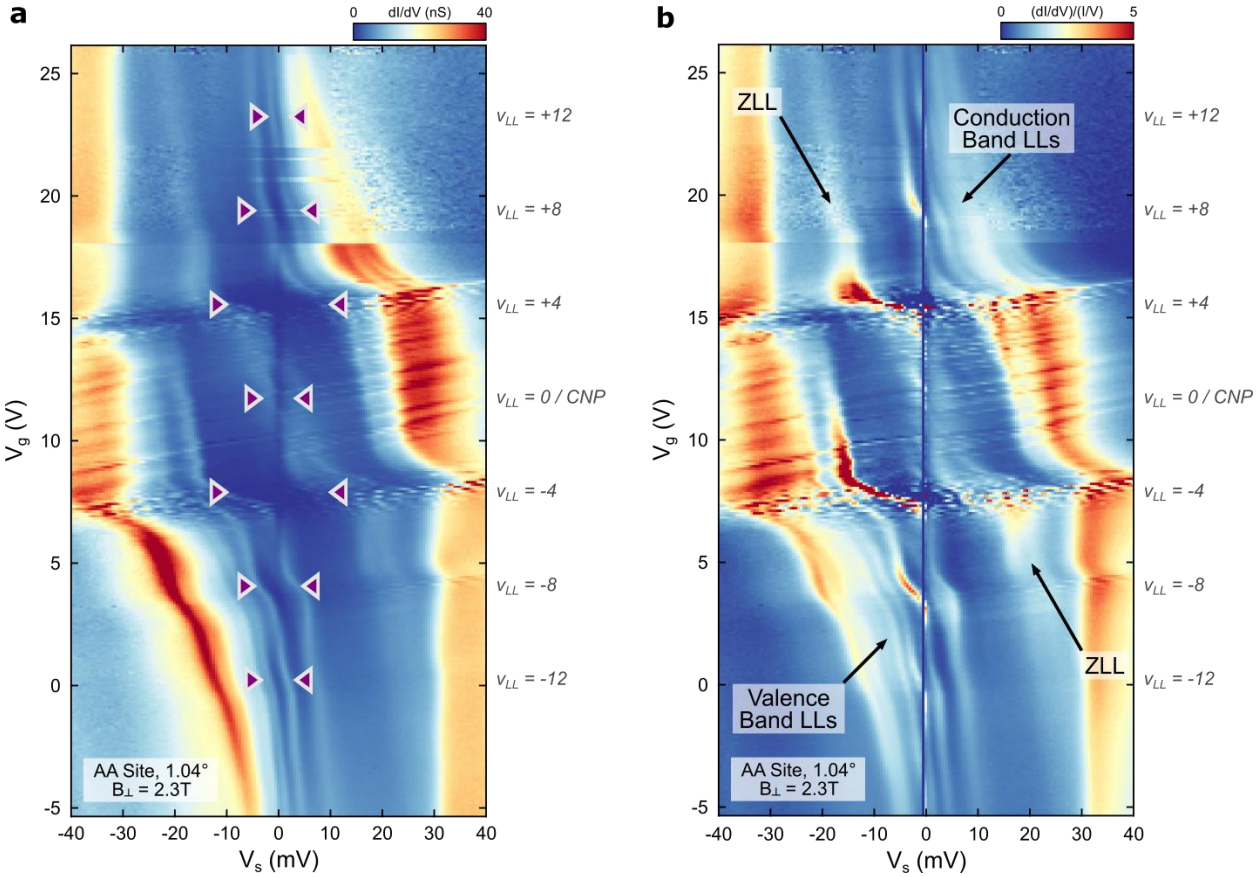

Figure S3 | Higher-index Landau levels near charge neutrality. a, d*I*/d*V*(V_s,V_g) measured at the center of an AA site in Device B at B = 2.3 T (Initial tunneling parameters: V_s = -80 mV, I = 1.0 nA, 381.7 Hz sinusoidal modulation at V_{rms} = 500 μV). The markers on the right side of the plot indicate the LL filling, as measured by the gate voltages at which LL gaps are seen at the Fermi energy. Purple triangles mark gaps at E_F. **b,** Same as **a** except normalized by dividing by I/V_s.

SUPPLEMENTARY FIGURE S4

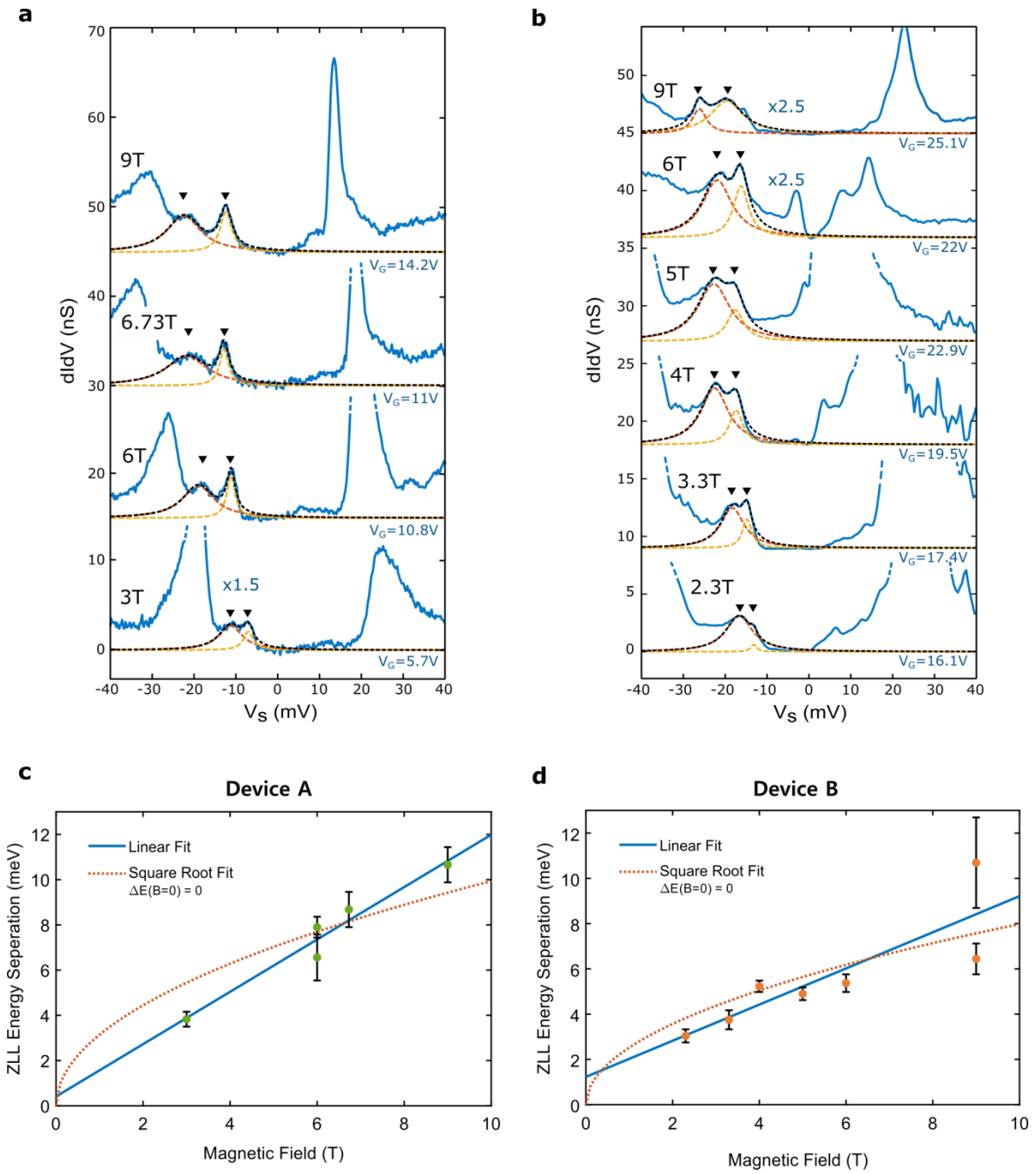

Figure S4 | Linear in magnetic-field dependence of the ZLL quartet splitting. a,b, Representative d*I*/d*V*(V_s) spectra at each field in Device A (**a**) and Device B (**b**) showing the single-particle energy separation of the ZLLs, as observed away from E_F. **c,d,** Summary of the single-particle energy splitting as a function of magnetic field in Device A (**c**) and Device B (**d**). Device A shows a clear linear dependence on magnetic field strength, while the functional dependence of the data from Device B appears inconclusive.

SUPPLEMENTARY FIGURE S5

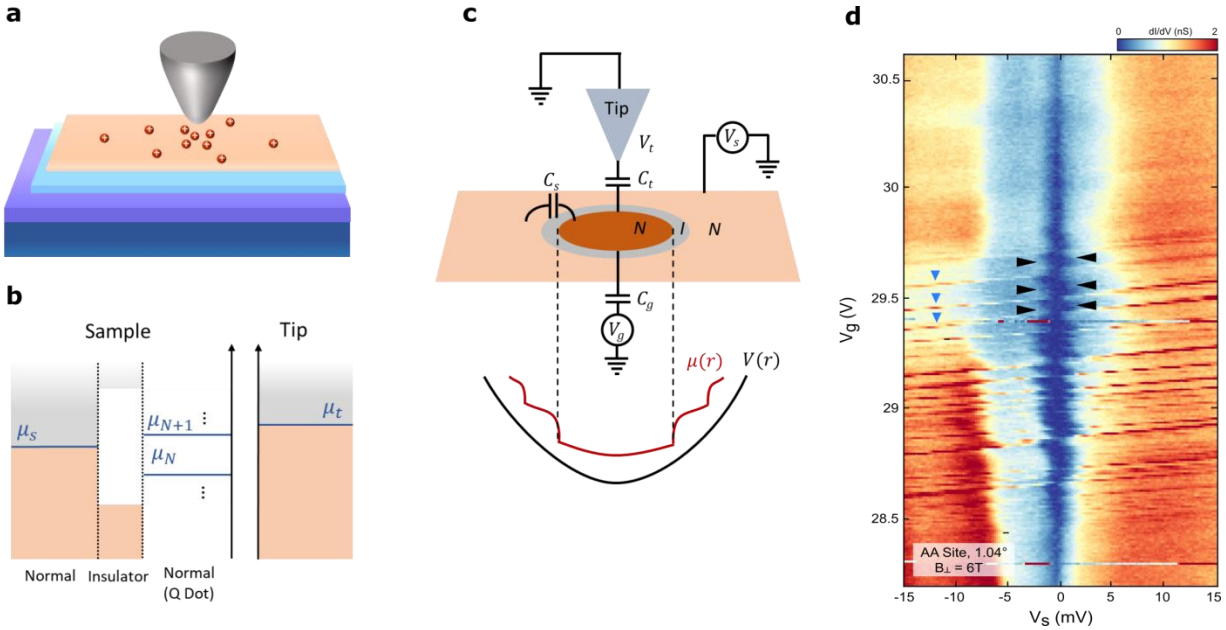

Figure S5 | Effects of local STM tip potential on spectroscopic gap measurements: charging energy and Coulomb diamonds.

a, Schematic drawing of tip-induced gating effect, where a local electric field induced by a difference in electrostatic potential leads to a spatially-dependent charge distribution in the sample. **b,** Schematic diagram of the tunneling junction geometry of the quantum dot model described in the Supplementary Section E. **c,** Schematic circuit drawing of the quantum dot model. $V(r)$ represents a confining potential induced by the tip-gating effect, which causes an insulating ring (I) to form between non-insulating regions (N) in the presence of a spatially varying chemical potential. **d,** $dI/dV(V_s,V_g)$ measured at the center of an AA site in Device B at 6 T (Initial tunneling parameters: V_s = -90 mV, I = 600 pA, 381.7 Hz sinusoidal modulation at V_{rms} = 200 μV). Labeled in this data are the charging lines (blue triangles) and Coulomb-diamond-like features (black triangles) observed in spectroscopy near a strongly correlated Chern insulating gap with Chern number +3 near filling +1.

SUPPLEMENTARY FIGURE S6

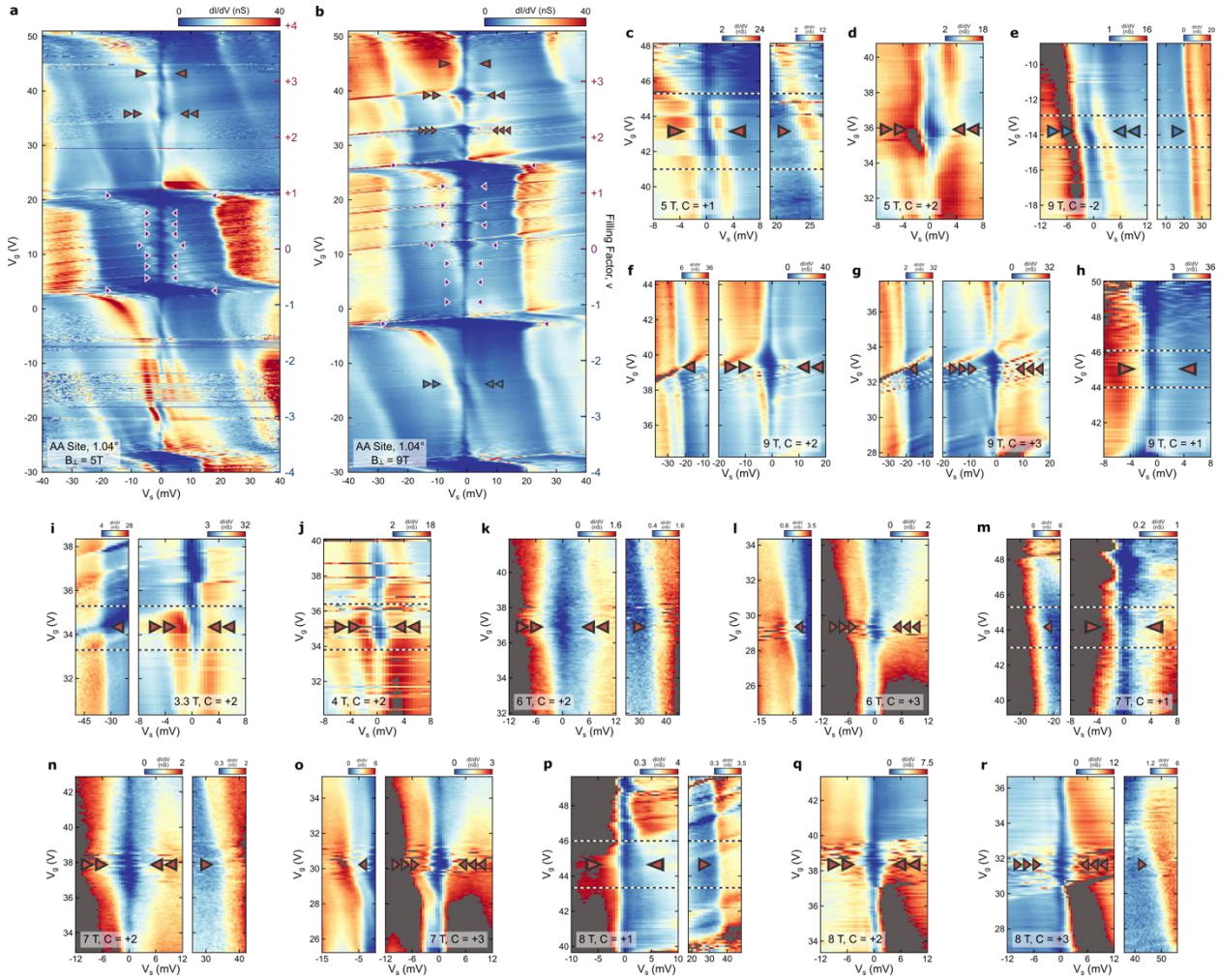

Figure S6 | Raw d*I*/d*V*(V_s, V_g) as a function of magnetic field for Device B at T = 300 mK. a, d*I*/d*V*(V_s,V_g) measured at the center of an AA site at B = 5 T (Initial tunneling parameters: V_s = -80 mV, I = 1.0 nA, 381.7 Hz sinusoidal modulation at V_{rms} = 500 μV). Red arrows identify strongly correlated Chern insulating gaps near fillings +3 and +2, with Chern numbers +1 and +2 respectively. Purple arrows identify the ZLL gaps at LL fillings –4 to +4. **b,** d*I*/d*V*(V_s,V_g) measured at the center of an AA site at B = 9 T (Initial tunneling parameters: V_s = +80 mV, I = 900 pA, 381.7 Hz sinusoidal modulation at V_{rms} = 500 μV). Red arrows identify strongly correlated Chern insulating gaps emanating from fillings +3, +2, and +1, with Chern numbers +1, +2, and +3 respectively. Blue arrows identify a strongly correlated Chern insulating gap emanating from fillings -2, with Chern number -2. Purple arrows identify the ZLL gaps at LL fillings –4 to +4. **c**-**r**, Zoomed-in d*I*/d*V*(V_s,V_g) plots of various Chern gaps for various values of the magnetic field. A nearby band edge is also shown for **c**, **e**-**g**, **i**, **k**-**p**, and **r**, which each shows a sudden shift in the energy of the band that signals a change in the chemical potential commensurate with the gap opening. Dashed lines, if shown, indicate the error bar for the gap.

SUPPLEMENTARY FIGURE S7

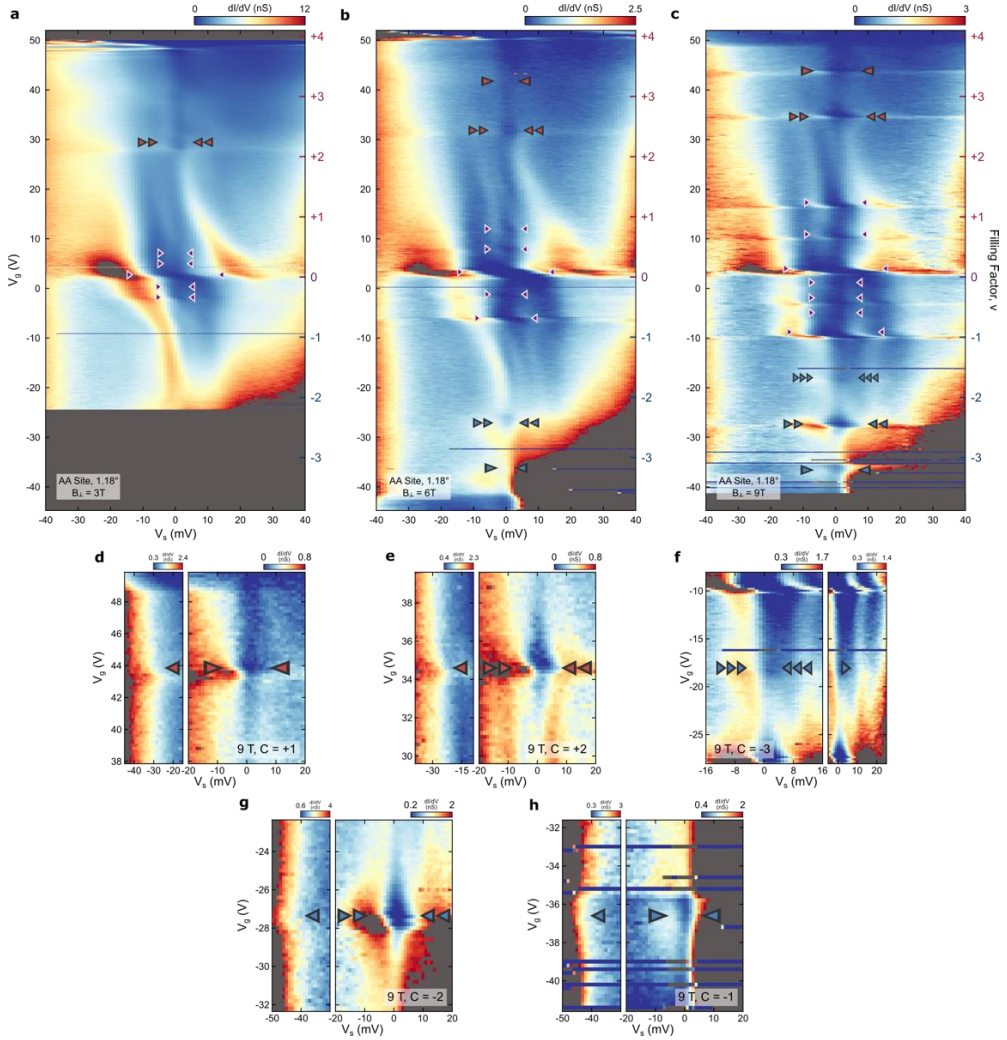

Figure S7 | Raw d*I*/d*V*(V_s, V_g) as a function of magnetic field for Device C at T = 6.5 K. a, d*I*/d*V*(V_s,V_g) measured at the center of an AA site at B = 3 T. Red arrows identify a strongly correlated Chern insulating gaps near fillings +2 with Chern number +2. Purple arrows identify the ZLL gaps at LL fillings -4, -2, 0, +2, and +4. **b,** d*I*/d*V*(V_s,V_g) measured at the center of an AA site at B = 6 T. Red arrows identify strongly correlated Chern insulating gaps emanating from fillings +3 and +2, with Chern numbers +1 and +2 respectively. Blue arrows identify strongly correlated Chern insulating gaps emanating from fillings -2 and -3, with Chern numbers -2 and -1 respectively. Purple arrows identify the ZLL gaps at LL fillings -4, -2, 0, +2, and +4. **c,** d*I*/d*V*(V_s,V_g) measured at the center of an AA site at B = 9 T. Red arrows identify strongly correlated Chern insulating gaps near fillings +3 and +2, with Chern numbers +1 and +2 respectively. Blue arrows identify strongly correlated Chern insulating gaps near fillings -1, -2, and -3, with Chern numbers -3, -2, and -1 respectively. Purple arrows identify the ZLL gaps at LL fillings –4, -3, -2, -1, 0, +2, and +4. Initial tunneling parameters: V_s = -80 mV; I = 1.5 nA (**a**), 500 pA (**b**,**c**); 381.7 Hz sinusoidal modulation at V_{rms} = 1 mV. **d**-**h**, Zoomed-in d*I*/d*V*(V_s,V_g) plots of the Chern gaps for B = 9 T. A nearby band edge is also shown for each gap.

SUPPLEMENTARY FIGURE S8

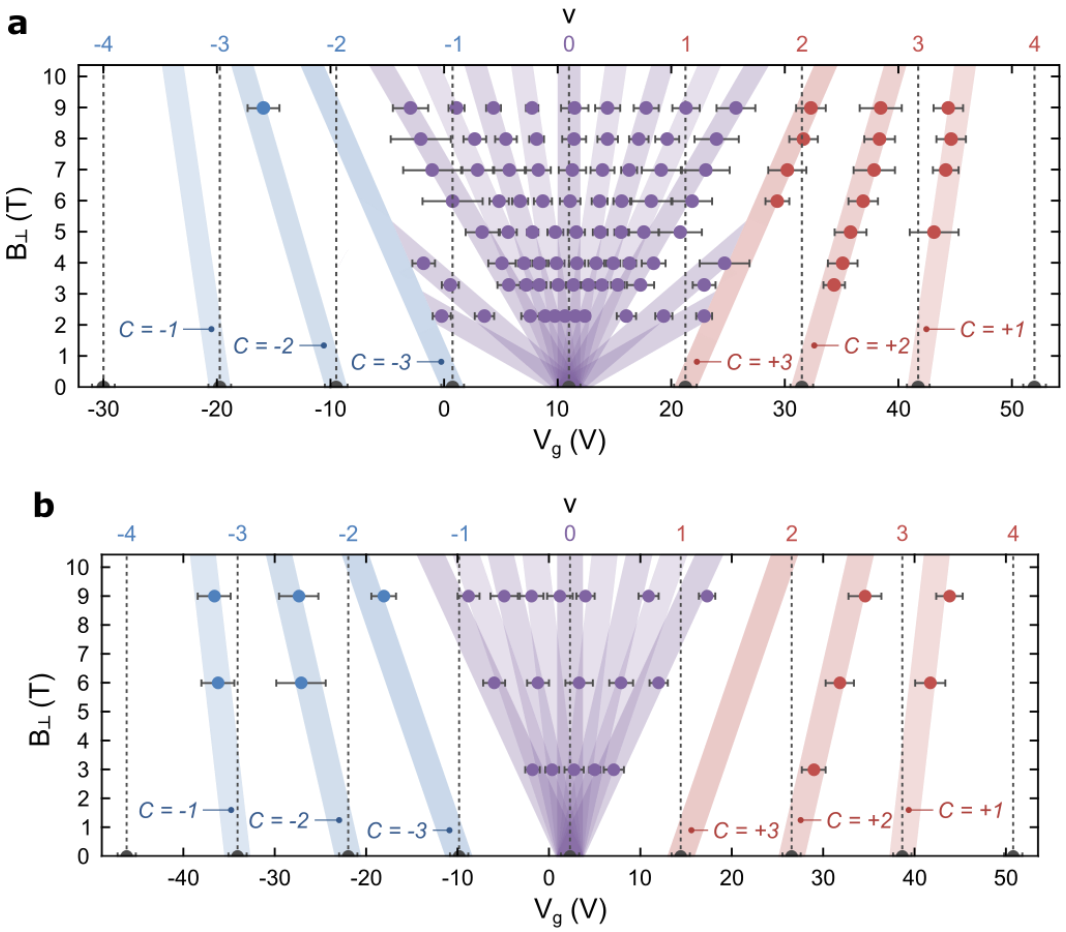

Figure S8 | Quantized field response of strongly correlated Chern insulating phases in Devices B and C. a, Scatter plot of gate voltage as a function of magnetic field for extracted spectroscopic gaps from d*I*/d*V*(V_s,V_g) measurements on Device B. Purple shaded bars depict expected quantized field response of LL gaps with LL filling factors $\nu_{LL} \in [-4, +4]$. Red and blue shaded bars depict expected quantized field response of Chern insulating gaps with C = ±1, ±2, ±3 emanating integer flat-band fillings ν = ±3, ±2, ±1, respectively. The width of the shaded bars is derived from the error in determining band full (ν = +4) and empty (ν = -4) fillings, between which all integer fillings ν were defined to be equally spaced. **b,** Same as **a** for the measurements performed on Device C.

SUPPLEMENTARY FIGURE S9

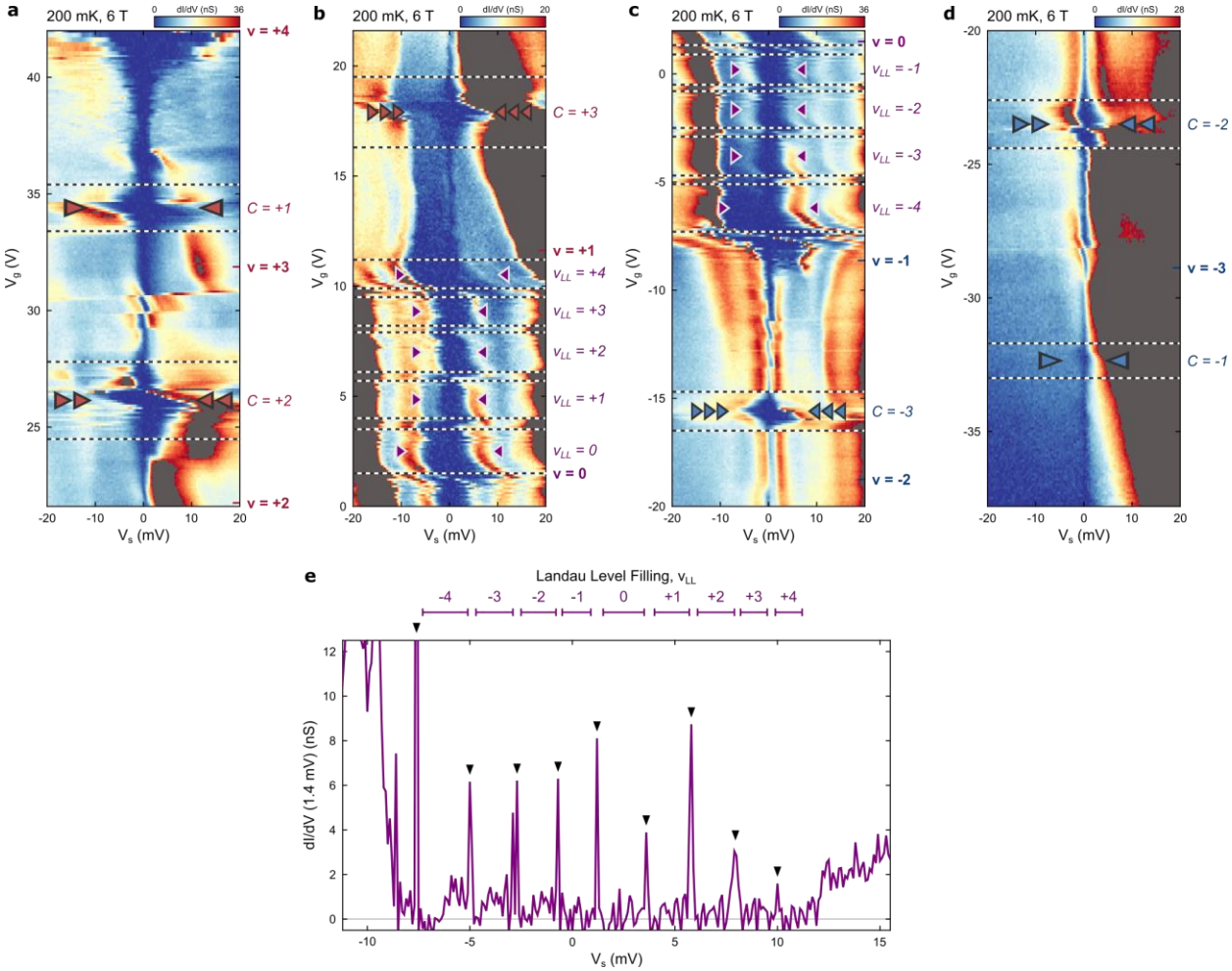

Figure S9 | Spectroscopic gap location and error extraction in example from main text Fig. 1d. a-d, d*I*/d*V*(V_s,V_g) measured at the center of an AA site in Device A at B = 6 T. The dashed lines enclose the LL and SCCI gaps and define the gate-voltage error bars used in the extracted gap information plotted in main text Figs. 3a,b. **e**, d*I*/d*V* near zero bias (V_s = 1.4 mV) showing peaks that appear when a LL crosses E_F. The purple data points in main text Fig. 3a (and purple triangles in **b** and **c**) are defined to be halfway between peaks, with error bars encompassing the full widths between peaks.

SUPPLEMENTARY FIGURE S10

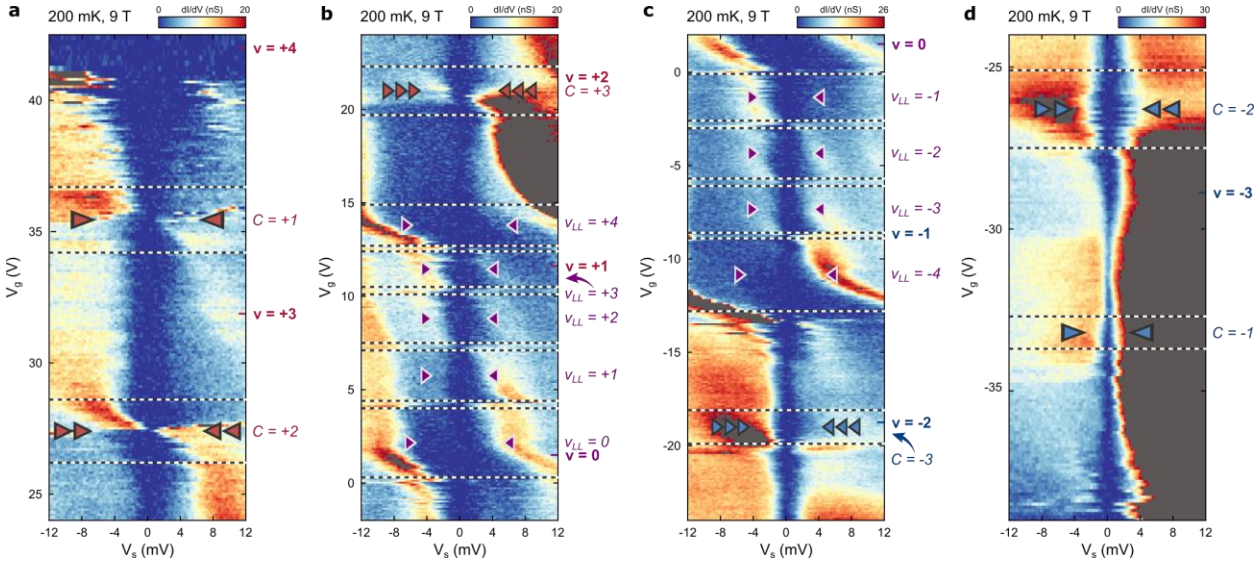

Figure S10 | Spectroscopic gap location and error extraction in example from main text Fig. 1e. a-d, d*I*/d*V*(V_s,V_g) measured at the center of an AA site in Device A at B = 9 T. The dashed lines enclose the LL and SCCI gaps and define the gate-voltage error bars used in the extracted gap information plotted in main text Figs. 3a,b.

SUPPLEMENTARY FIGURE S11

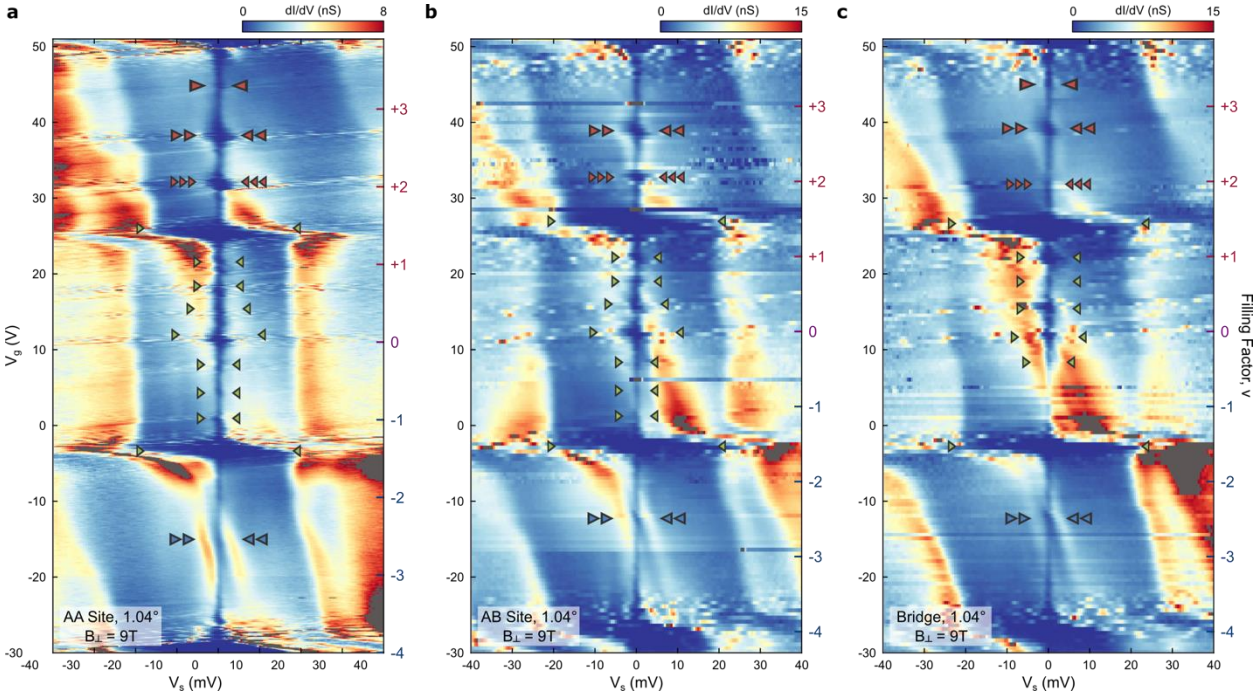

Figure S11 | Strongly correlated Chern insulating gaps and zeroth Landau level gaps observed at different locations in the moiré superlattice. a,b,c, d*I*/d*V*(V_s,V_g) measured at the center of an AA site (**a**), AB / BA site (**b**), and a bridge site (**c**) in Device B at B = 9 T.

SUPPLEMENTARY FIGURE S12

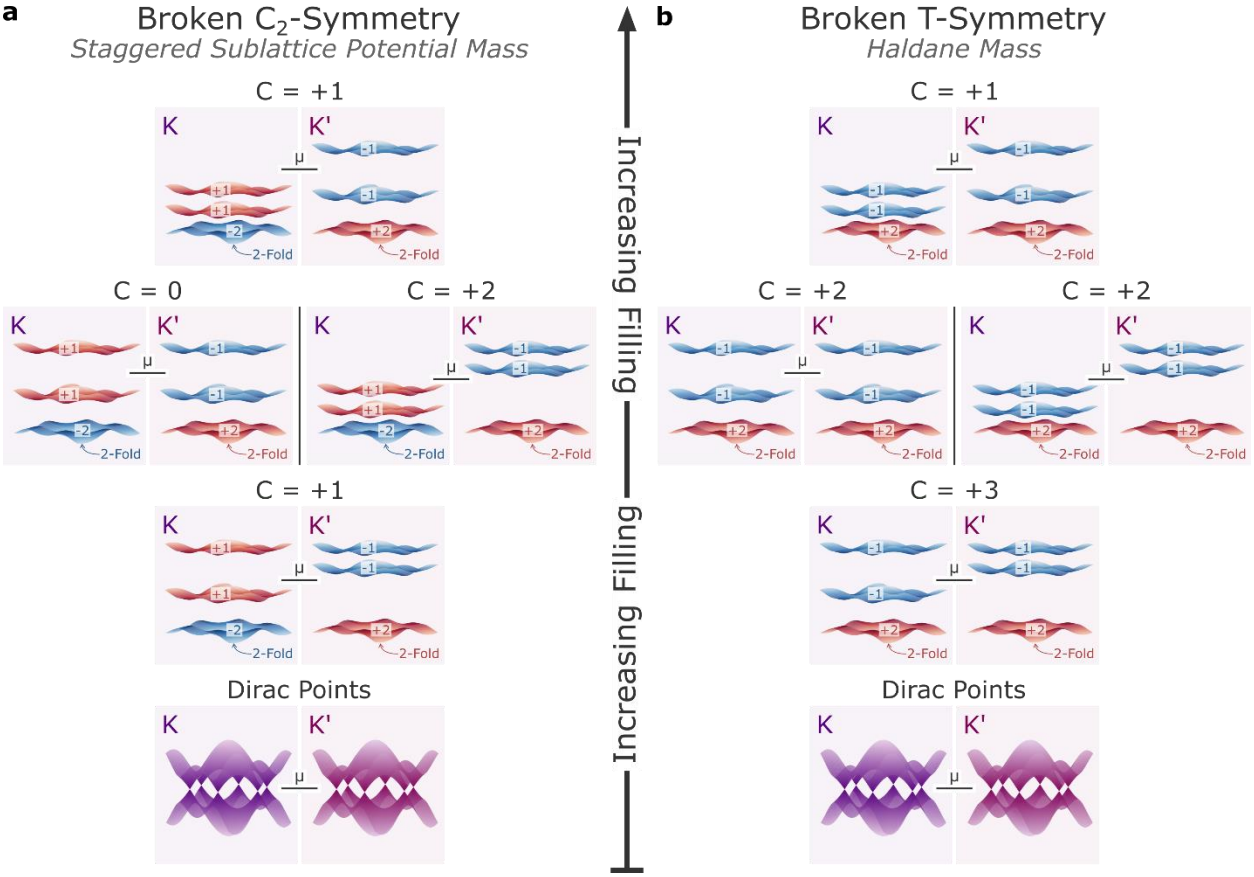

Figure S12 | Chern insulating states: Staggered potential mass vs. Haldane mass. a, Schematic diagram of the expected Chern phases in C_2-symmetry-broken MATBG near fillings $\nu = +3$ (top), $\nu = +2$ (upper middle), and $\nu = +1$ (lower middle). Band labels indicate the Chern numbers of each sub-band / pair of degenerate sub-bands. In the presence of an interaction-induced staggered sublattice potential mass, insulating states with Chern numbers $C = \pm 1, 0$ or $\pm 2, \pm 1$ form near integer fillings $\nu = \pm 3, \pm 2, \pm 1$**. b,** Schematic diagram of the expected Chern phases in T-symmetry-broken MATBG near fillings $\nu = +3$ (top), $\nu = +2$ (upper middle), and $\nu = +1$ (lower middle). In the presence of an interaction-induced Haldane mass, insulating states with Chern numbers $C = \pm 1, \pm 2, \pm 3$ form near integer fillings $\nu = \pm 3, \pm 2, \pm 1$**.**

SUPPLEMENTARY FIGURE S13

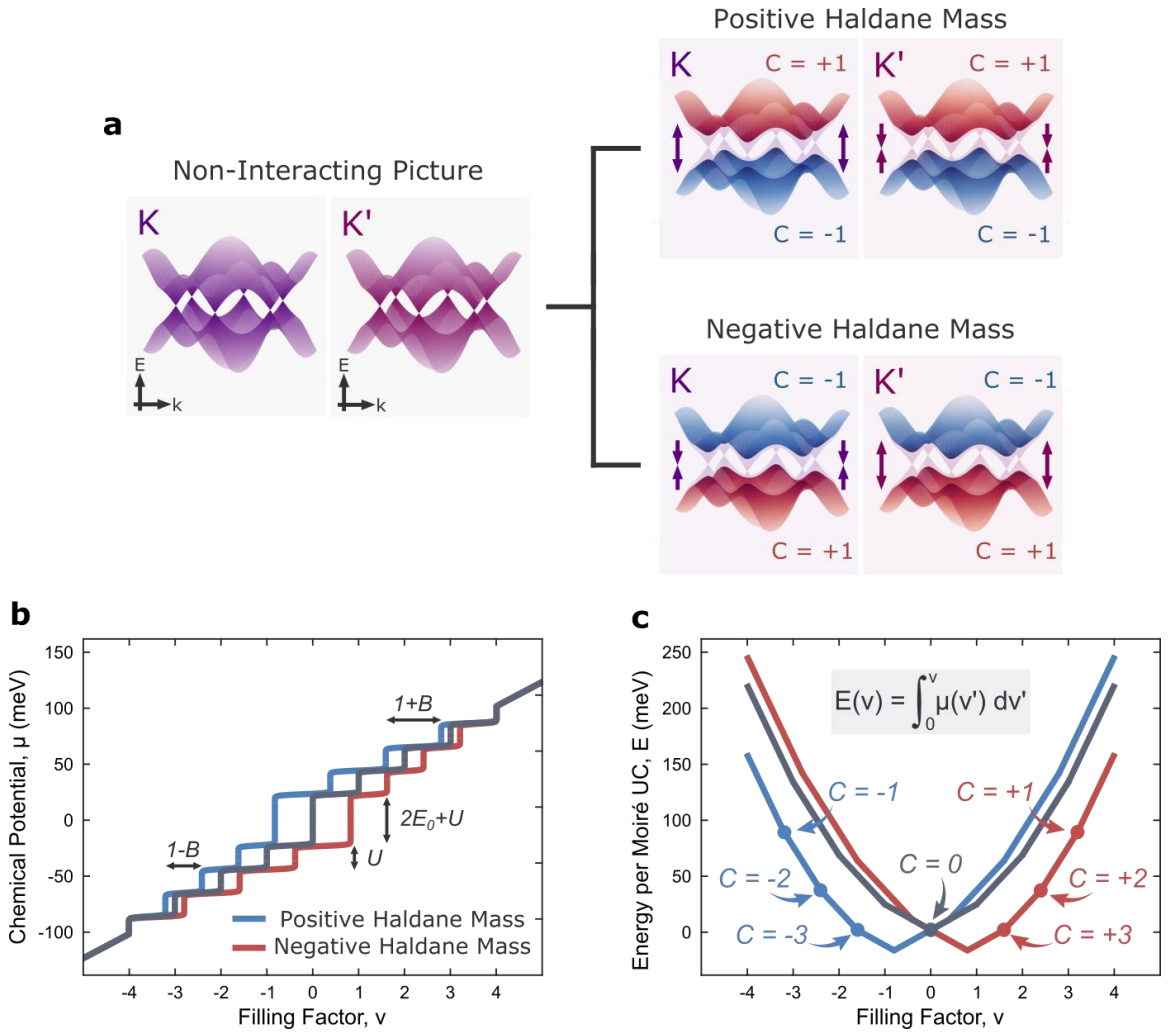

Figure S13 | Free energy argument for extremal Chern number phases. a, Schematic diagram of the influence of a positive (top) or negative (bottom) Haldane mass on the single-particle band picture of MATBG. **b,** Chemical potential μ as a function of filling ν at zero magnetic field (gray) or at finite magnetic field with a positive (blue) or negative (red) Haldane mass. Values of E_0 = 12.3 meV, U = 21.1 meV, and B = 0.2 were chosen for this schematic diagram to be broadly consistent with values extracted from the comparison of experimental measurements (Fig. 1e) to the phenomenological model discussed in Supplementary Section M. **c,** Energy per moiré unit cell E(ν) as a function of filling ν. States with positive (negative) Chern numbers, which exist when the Haldane mass is negative (positive), are lowest in energy.

SUPPLEMENTARY FIGURE S14

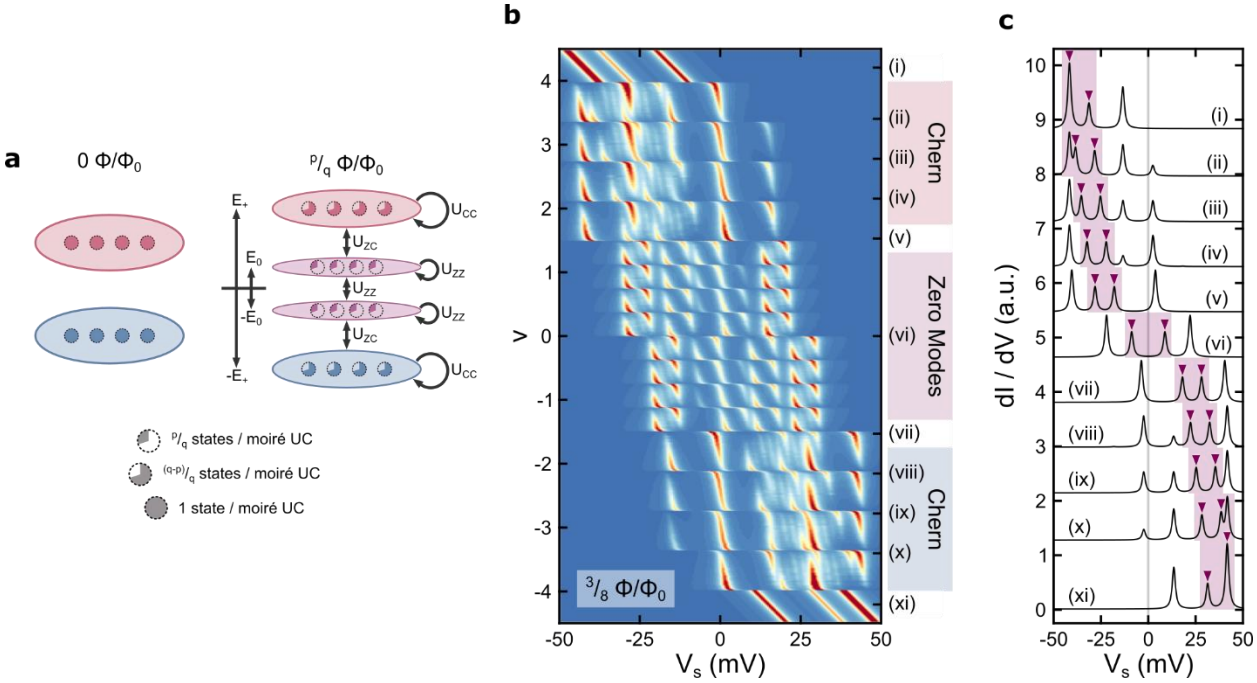

Figure S14 | Mean-field interaction model of Coulomb repulsion energy at high magnetic Fields. a, Schematic diagram of perfectly flat band mean-field model. At zero magnetic field, the upper (red) and lower (blue) flat bands each hold 4 states per moiré unit cell. At finite field, states transfer from these bands to new zeroth Landau levels (purple). Depicted are single-particle and mean-field interactions between various bands used in this model. **b,** Simulated d*I*/d*V*(V_s,V_g) using the described mean-field interaction model. Simulation parameters: $B/n_0 = \frac{3}{8}\Phi_0$, $U_{CC} = 15.6$ meV, $U_{CZ} = 7.6$ meV, $U_{ZZ} = 7.4$ meV, $E_+ = 14$ meV, $E_0 = 5$ meV. **c**, Simulated d*I*/d*V* line cuts taken from **b** (spectra labels correspond to regions labeled on the right side of **b**) that show the shifting zeroth Landau levels (highlighted in purple), which move from the valence flat band to the conduction flat band as MATBG shifts from n-doped to p-doped.